JACS
JOURNAL OF THE AMERICAN CHEMICAL SOCIETY

Article

pubs.acs.org/JACS

$[XeOXeOXe]^{2+}$, the Missing Oxide of Xenon(II); Synthesis, Raman Spectrum, and X-ray Crystal Structure of $[XeOXeOXe][\mu\text{-}F(ReO_2F_3)_2]_2$

Maria V. Ivanova, Hélène P. A. Mercier, and Gary J. Schrobilgen*

Department of Chemistry, McMaster University, Hamilton, Ontario L8S 4M1, Canada

Supporting Information

ABSTRACT: The $[XeOXeOXe]^{2+}$ cation provides an unprecedented example of a xenon(II) oxide and a noble-gas oxocation as well as a rare example of a noble-gas dication. The $[XeOXeOXe]^{2+}$ cation was synthesized as its $[\mu\text{-}F(ReO_2F_3)_2]^-$ salt by reaction of ReO_3F with XeF_2 in anhydrous HF at −30 °C. Red-orange $[XeOXeOXe][\mu\text{-}F(ReO_2F_3)_2]_2$ rapidly decomposes to XeF_2, ReO_2F_3, Xe, and O_2 when the solid or its HF solutions are warmed above −20 °C. The crystal structure of $[XeOXeOXe][\mu\text{-}F(ReO_2F_3)_2]_2$ consists of a planar, zigzag-shaped $[XeOXeOXe]^{2+}$ cation (C_{2h} symmetry) that is fluorine bridged through its terminal xenon atoms to two $[\mu\text{-}F(ReO_2F_3)_2]^-$ anions. The Raman spectra of the natural abundance and ^{18}O-enriched $[XeOXeOXe]^{2+}$ salts are consistent with a centrosymmetric (C_{2h}) cation geometry. A proposed reaction pathway leading to $[XeOXeOXe][\mu\text{-}F(ReO_2F_3)_2]_2$ consists of a series of oxygen/fluorine metathesis reactions that are presumably mediated by the transient HOXeF molecule. Quantum-chemical calculations were used to aid in the vibrational assignments of $[Xe^{16/18}OXe^{16/18}OXe][\mu\text{-}F(Re^{16/18}O_2F_3)_2]_2$ and to assess the bonding in $[XeOXeOXe]^{2+}$ by NBO, QTAIM, ELF, and MEPS analyses. Ion pair interactions occur through $Re{-}F_\mu{\cdots}Xe$ bridges, which are predominantly electrostatic in nature and result from polarization of the F_μ-atom electron densities by the exposed core charges of the terminal xenon atoms. Each xenon(II) atom is surrounded by a torus of xenon valence electron density comprised of the three valence electron lone pairs. The positive regions of the terminal xenon atoms and associated fluorine bridge bonds correspond to the positive σ-holes and donor interactions that are associated with "halogen bonding".

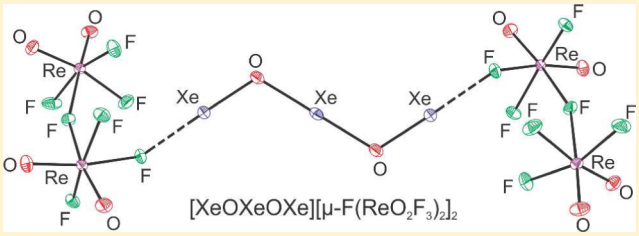

INTRODUCTION

Noble-gas compounds have generated considerable interest since the discovery of noble-gas reactivity by Neil Bartlett in 1962.[1] Over the ensuing decades, the syntheses of the binary xenon fluorides, KrF_2, and oxide fluorides of xenon have provided a diverse derivative chemistry.[2] Although thermodynamically unstable with respect to their elements, xenon oxides have also been isolated and characterized in macroscopic quantities for every known oxidation state of xenon except the $+^1/_2$ and +2 oxidation states, i.e., $Xe^{IV}O_2$,[3] $Xe^{VI}O_3$,[4−9] $Xe^{VIII}O_4$,[10−16] $(\eta^2\text{-}O_2)Xe^{VIII}O_3$,[16] and $[Xe^{VIII}O_6]^{4-}$.[7,17−34] No isolable oxides of krypton are known.[35] Both XeO_3 and XeO_4 are shock sensitive, decomposing explosively with the release of 402[6] and 642[12] kJ mol^{-1}, respectively, whereas water-insoluble XeO_2 quiescently decomposes under water at 0 °C[2] over several minutes. In contrast, $[Xe^{VIII}O_6]^{4-}$ salts are kinetically and thermodynamically stable at ambient temperatures and pressures[7] and have been characterized by X-ray crystallography,[17−22,25] Raman,[26,27,33] infrared,[23,26,33] photoelectron,[28,33] Auger,[28] Mössbauer,[30] ^{129}Xe NMR,[29,34] and UV[32] spectroscopy. Xenon tetroxide is generated by the reaction of concentrated H_2SO_4 with $Na_4[XeO_6]$ and has been isolated as a pale yellow, volatile solid, and its molecular structure has been obtained from an electron diffraction study of XeO_4 in the gas phase.[13] Xenon tetroxide has also been characterized by infrared,[10,16] Raman,[14,15] $^{129,131}Xe$ NMR spectroscopy,[15] and mass spectrometry.[11] Photolysis of XeO_4 in noble-gas matrices at 365 nm yielded the Xe(VIII) peroxo-compound, $(\eta^2\text{-}O_2)XeO_3$ and XeO_3.[16] The former was characterized by infrared spectroscopy. Xenon trioxide, XeO_3, has been synthesized as a colorless crystalline solid and characterized by single-crystal X-ray diffraction,[5] Raman,[8] and infrared[9] spectroscopy. Recently, XeO_2 has been synthesized as a bright yellow solid at 0 °C.[3] The characterization of XeO_2 by Raman spectroscopy revealed that XeO_2 is polymeric, possessing an extended structure in which Xe is bonded to four oxygen atoms having a local square-planar XeO_4 geometry around the central Xe atom.

The xenon(II) oxide, XeO, has been postulated as an intermediate in some oxidation reactions of XeO_3.[7] Its gas-phase UV and vacuum UV emission spectra have been attributed to emissions from Xe^+O^- ion pair states.[36,37] Monomeric XeO has not been synthesized in macroscopic amounts, but has been obtained in an argon matrix[38] where UV spectroscopic evidence suggested that the ground state of XeO is essentially a van der Waals molecule with a bond length considerably longer than the excited state value. Xenon monoxide was subsequently shown by gas-phase quantum-chemical calculations to have an unbound $^3\Pi$ ground state. The only bound state is the excited $1^1\Sigma^+$ state.[36,37]

Received: August 18, 2015
Published: September 22, 2015

DOI: 10.1021/jacs.5b08765
J. Am. Chem. Soc. 2015, 137, 13398−13413

Scheme 1. Proposed Reaction Pathway Leading to the Formation of $[XeOXeOXe][\mu\text{-}F(ReO_2F_3)_2]_2$

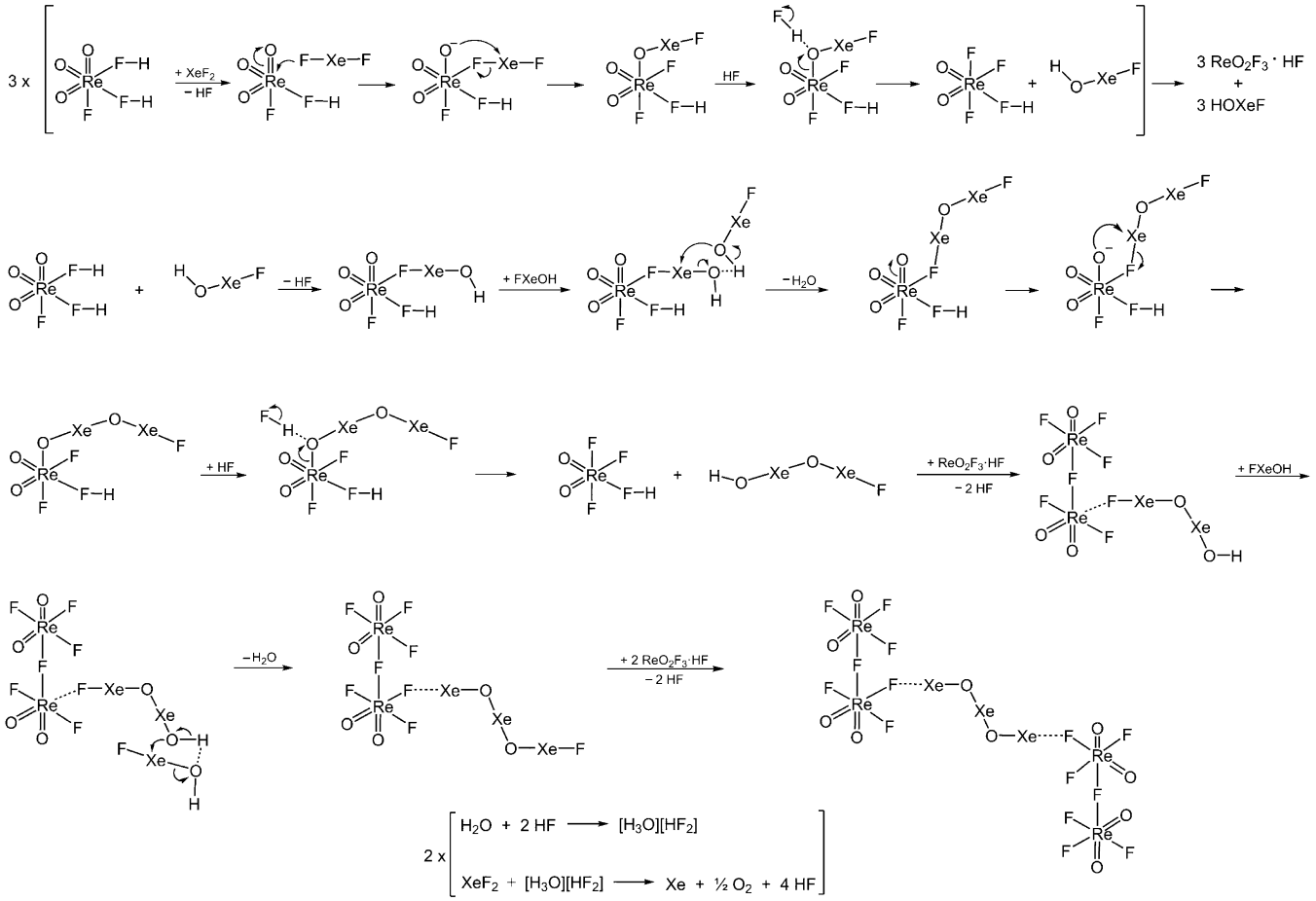

In a prior study, the first xenon(II) oxide fluoride species, $[FXeOXeFXeF]^+$, was synthesized as its $[PnF_6]^-$ (Pn = As, Sb) salts by reaction of XeF_2 with $[H_3O][PnF_6]$ in HF.[39] The $[FXeOXeFXeF][PnF_6]$ salts were characterized by single-crystal X-ray diffraction, Raman spectroscopy, and quantum-chemical calculations. Although the oxygen and fluorine atoms bonded to the central Xe atom of $[FXeOXeFXeF]^+$ are positionally disordered in both $[PnF_6]^-$ salts, the presence of a bridging oxygen atom was corroborated by $^{16/18}O$ isotopic shifts obtained from the Raman spectrum and by isotopic shift values obtained from quantum-chemical calculations. It was proposed that XeF_2 is hydrolyzed by $[H_3O]^+$ to form FXeOH, an intermediate in the formation of the $[FXeOXeFXeF]^+$ cation.

In the quest for a xenon(II) oxide, the reaction of ReO_3F with XeF_2 was investigated as a possible means to transfer oxygen to xenon(II). A reliable synthesis of high-purity ReO_3F in anhydrous HF (aHF) has been recently developed,[40] which has allowed its chemistry to be more widely explored. The HF solvate, $ReO_3F(FH)_2$, has also been isolated and characterized by single-crystal X-ray diffraction and Raman spectroscopy.

The present study reports the synthesis and characterization of the first xenon(II) oxide, $[XeOXeOXe]^{2+}$ as its $[\mu\text{-}F(ReO_2F_3)_2]^-$ salt. The salt has been structurally characterized by low-temperature single-crystal X-ray diffraction and Raman spectroscopy. Vibrational assignments have been made with the aid of quantum-chemical calculations, which were supported by ^{18}O-enrichment studies. The nature of the bonding in $[XeOXeOXe][\mu\text{-}F(ReO_2F_3)_2]_2$ has been examined using natural bond orbital (NBO), quantum theory of atoms in molecules (QTAIM), electron localization function (ELF), and molecular electrostatic potential surface (MEPS) analyses.

RESULTS AND DISCUSSION

Synthesis of $[XeOXeOXe][\mu\text{-}F(ReO_2F_3)_2]_2$. Reaction progress and product purities were monitored by recording the Raman spectra of the solids under aHF in FEP reaction vessels at −140 °C.

The salt, $[XeOXeOXe][\mu\text{-}F(ReO_2F_3)_2]_2$, was obtained by the reaction of ReO_3F[40] with XeF_2 in aHF at −30 °C according to a three-step reaction sequence (eqs 1−3), with the overall synthesis summarized in eq 4. A range of XeF_2:$ReO_3F(FH)_2$ molar ratios was surveyed to determine whether or not other xenon(II) oxide or oxide fluoride cations could be formed.

$$ReO_3F + 2HF \rightarrow ReO_3F(FH)_2 \quad (1)$$

$$3XeF_2 + 4ReO_3F(FH)_2 \rightarrow [XeOXeOXe][\mu\text{-}F(ReO_2F_3)_2]_2 + 2[H_3O][HF_2] \quad (2)$$

$$2XeF_2 + 2[H_3O][HF_2] \rightarrow 2Xe + O_2 + 8HF \quad (3)$$

$$5XeF_2 + 4ReO_3F(FH)_2 \rightarrow [XeOXeOXe][\mu\text{-}F(ReO_2F_3)_2]_2 + 2Xe + O_2 + 8HF \quad (4)$$

DOI: 10.1021/jacs.5b08765
J. Am. Chem. Soc. 2015, 137, 13398−13413

The molar ratios of the reactants, XeF_2:ReO_3F, were 2.11:1.00, 1.19:1.00, 1.18:1.00, 1.14:1.00, 1.02:1.00, and 0.56:1.00. Upon warming the reaction mixtures to −30 °C, ReO_3F and XeF_2 dissolved in aHF over a period of ca. 5−10 min, forming pale yellow solutions. As the reactions progressed over a period of 2−4 h at −30 °C, the solution colors changed from pale yellow to yellow-orange. Rapid cooling of the solutions (XeF_2:ReO_3F = 2.11:1.00, 1.19:1.00, 1.18:1.00, 1.14:1.00) to −78 °C resulted in irreversible precipitation of red-orange colored microcrystalline powders that was accompanied by solution color changes from yellow-orange to colorless upon complete precipitation. The low-temperature Raman spectra of the red-orange crystalline products under frozen aHF (XeF_2:ReO_3F = 1.19:1.00, 1.14:1.00) and products isolated under dynamic vacuum at −78 °C (XeF_2:ReO_3F = 2.11:1.00, 1.18:1.00) were identical and were assigned to $[XeOXeOXe][\mu\text{-}F(ReO_2F_3)_2]_2$. Crystals of $[XeOXeOXe][\mu\text{-}F(ReO_2F_3)_2]_2$ that were of a quality suitable for an X-ray structure determination were grown by slowly cooling the yellow-orange solutions (XeF_2:ReO_3F = 0.56:1.00 and 1.02:1.00) from −30 to −35 °C over a 5 h period. The ^{18}O-enriched salt, $[Xe^{18}OXe^{18}OXe][\mu\text{-}F(Re^{18}O_2F_3)_2]_2$, was also synthesized from enriched $Re^{18}O_3F$ using a modification of a published synthetic procedure[40] (also see Experimental Section).

A plausible reaction pathway leading to $[XeOXeOXe][\mu\text{-}F(ReO_2F_3)_2]_2$ is provided in Scheme 1. The reaction sequence is presumably initiated by XeF_2 coordination to $ReO_3F(FH)_2$, followed by intramolecular rearrangements that lead to $[OXeFReO_2F_2(FH)]$. Subsequent HF solvolysis yields $ReO_2F_3(FH)$ and HOXeF. The HOXeF molecule has also been invoked as a key reaction intermediate in the synthesis of the $[FXeOXeFXeF]^+$ cation.[39] The reaction of HOXeF with a second equivalent of $ReO_3F(FH)_2$ provides $[HOXeFReO_3F(FH)]$, which, in turn, undergoes condensation with HOXeF to yield $[FXeOXeFReO_3F(FH)]$. The latter product undergoes intramolecular rearrangement and subsequent HF solvolysis to form $ReO_2F_3(FH)$ and FXeOXeOH. Fluorine coordination of FXeOXeOH to Lewis acidic μ-$F(ReO_2F_3)(ReO_2F_2)$ results in a positive charge on the XeOXeOH unit of μ-F(XeOXeOH)[μ-$F(ReO_2F_3)(ReO_2F_2)$] which promotes a further FXeOH condensation/H_2O elimination reaction to give μ-F[FXeOXeOXe][μ-$F(ReO_2F_3)$-(ReO_2F_2)]. In view of the stabilities of $[\mu\text{-}F(ReO_2F_3)_2]^-$ salts,[41] the latter complex may be reformulated as $[FXeOXeOXe][\mu\text{-}F(ReO_2F_3)_2]$, where it is understood that there is a Xe---F−Re fluorine bridge interaction between the cation and the anion. In the final step, $[FXeOXeOXe]^+$ undergoes fluoride ion abstraction by 2 equiv of $ReO_2F_3(FH)$, which undergo HF elimination to give $[XeOXeOXe][\mu\text{-}F(ReO_2F_3)_2]_2$. Water generated in Scheme 1 is protonated in HF,[42,43] forming $[H_3O][HF_2]$ which reacts with XeF_2 according to eq 3 to form Xe, O_2, and HF. Although the $[FXeOXeFXeF]^+$ cation may be formed as an intermediate, its $[AsF_6]^-$ and $[SbF_6]^-$ salts have been shown to rapidly decompose, with gas evolution, above −30 °C.[39]

The $[XeOXeOXe][\mu\text{-}F(ReO_2F_3)_2]_2$ salt decomposes as a solid or in HF solvent to ReO_2F_3, XeF_2 (both confirmed by Raman spectroscopy), O_2, and Xe at temperatures above −20 °C (eq 5).

$$[XeOXeOXe][\mu\text{-}F(ReO_2F_3)_2]_2 \rightarrow 4ReO_2F_3 + XeF_2 + O_2 + 2Xe \quad (5)$$

Xenon formation was confirmed by condensation from the evolved gas mixture at −196 °C. In a separate study, ReO_2F_3 and XeF_2 were shown to be unreactive in aHF at room temperature and when equimolar amounts were fused at 80 °C. In instances (XeF_2:ReO_3F = 1.19:1.00, 1.14:1.00) where $[XeOXeOXe][\mu\text{-}F(ReO_2F_3)_2]_2$ had been isolated before the reaction sequence (eqs 2−4) had gone to completion (ca. 1h at −35 °C), the solution samples were allowed to decompose (−20 °C to room temperature) and were pumped on at room temperature to remove HF, XeF_2, Xe, and O_2. The Raman spectra of the resulting solids consisted of mixtures of ReO_2F_3 and unreacted ReO_3F.

X-ray Crystallography. Details of the data collection and other crystallographic information for $[XeOXeOXe][\mu\text{-}F(ReO_2F_3)_2]_2$ are given in Table 1, and important bond lengths and bond angles are provided in Tables 2 and S1, respectively.

Table 1. Summary of Crystal Data and Refinement Results for $[XeOXeOXe][\mu\text{-}F(ReO_2F_3)_2]_2$

$[XeOXeOXe][\mu\text{-}F(ReO_2F_3)_2]_2$	
space group	$P\bar{1}$
a (Å)	7.7142(2)
b (Å)	8.0991(2)
c (Å)	10.0494(2)
α (deg)	88.2797(13)
β (deg)	69.1278(12)
γ (deg)	62.0249(12)
V (Å)^3	510.91(2)
molecules/unit cell	1
mol wt (g mol^{-1})	1564.7
calcd density (g cm^{-3})	5.086
T (°C)	−173
μ (mm^{-1})	28.67
R_1[a]	0.0283
wR_2[b]	0.0597

[a] R_1 is defined as $\sum||F_o| - |F_c|| \sum|F_o|$ for $I > 2\sigma(I)$. [b] wR_2 is defined as $[\sum[w(F_o^2 - F_c^2)^2]/\sum w(F_o^2)^2]^{1/2}$ for $I > 2\sigma(I)$.

The salt, $[XeOXeOXe][\mu\text{-}F(ReO_2F_3)_2]_2$, crystallizes in the triclinic space group $P\bar{1}$ (Z = 1) (Figure 1). The unit cell consists of a well-isolated $[XeOXeOXe][\mu\text{-}F(ReO_2F_3)_2]_2$ ion pair, where the $[XeOXeOXe]^{2+}$ cation interacts through fluorine bridges with two symmetry-equivalent $[\mu\text{-}F(ReO_2F_3)_2]^-$ anions. The $[XeOXeOXe][\mu\text{-}F(ReO_2F_3)_2]_2$ ion pairs occupy parallel b,c-planes and stack along the a-axis (Figure S1). The shortest intermolecular ligand atom distances occur for $O_{(1)}\cdots O_{(4C)}$ (2.962(8) Å) and $F_{(7)}\cdots O_{(2K)}$ (2.882(8) Å), which are close to the corresponding sums of the van der Waals radii (O···O, 3.04 and O···F, 2.99 Å).[44] The central $Xe_{(1)}$ atom has six Xe···O (3.324(6)−3.663(6) Å) and four Xe···F (3.119(5)−3.429(5) Å) long contacts, and the terminal $Xe_{(2,2A)}$ atoms have two Xe···O (3.311(6), 3.239(6) Å) and five Xe···F (3.114(5)−3.419(5) Å) long contacts so that the total coordination numbers of $Xe_{(1)}$ and $Xe_{(2)}$ are 12 and 9, respectively (Figure S2). These contacts are somewhat shorter than the sums of the Xe···O (3.68 Å) and Xe···F (3.63 Å) van der Waals radii.[44] In the absence of these contacts, both xenon atoms are under bonded, having bond valences[45] of 1.56

DOI: 10.1021/jacs.5b08765
J. Am. Chem. Soc. 2015, 137, 13398−13413

Table 2. Experimental and Calculated Geometric Parameters for $[XeOXeOXe][\mu\text{-}F(ReO_2F_3)_2]_2$ (C_i), $[XeOXeOXe]^{2+}$ (C_{2h}), and FXeOXeOXeF (C_i)

	$[XeOXeOXe][\mu\text{-}F(ReO_2F_3)_2]_2$		$[XeOXeOXe]^{2+}$	FXeOXeOXeF		$[XeOXeOXe][\mu\text{-}F(ReO_2F_3)_2]_2$	
	exptl[a]	calcd[b]	calcd[b]			exptl[a]	calcd[b]
Bond Lengths (Å)					Bond Angles (deg)		
$Xe_{(1)}-O_{(1)}$	2.135(6)	2.174	2.207	2.155	$O_{(2)}-Re_{(1)}-F_{(2)}$	90.2(2)	91.6
$Xe_{(2)}-O_{(1)}$	1.987(6)	2.034	2.021	2.098	$O_{(2)}-Re_{(1)}-F_{(3)}$	96.4(2)	97.8
$Xe_{(2)}\cdots F_{(1)}$	2.392(4)	2.310		2.086	$O_{(2)}-Re_{(1)}-F_{(4)}$	96.4(3)	97.8
$Re_{(1)}-F_{(1)}$	2.007(4)	2.112			$F_{(1)}-Re_{(1)}-F_{(2)}$	77.5(2)	76.7
$Re_{(1)}-O_{(3)}$	1.676(6)	1.680			$F_{(1)}-Re_{(1)}-F_{(3)}$	82.4(2)	80.4
$Re_{(1)}-O_{(2)}$	1.673(6)	1.678			$F_{(1)}-Re_{(1)}-F_{(4)}$	81.5(2)	80.5
$Re_{(1)}-F_{(3)}$	1.859(4)	1.863			$F_{(2)}-Re_{(1)}-F_{(3)}$	80.5(2)	80.5
$Re_{(1)}-F_{(4)}$	1.852(5)	1.860			$F_{(2)}-Re_{(1)}-F_{(4)}$	82.7(2)	80.6
$Re_{(1)}-F_{(2)}$	2.048(4)	2.073			$F_{(3)}-Re_{(1)}-F_{(4)}$	158.8(2)	155.8
$Re_{(2)}-O_{(4)}$	1.750(5)	1.687			$Re_{(1)}-F_{(2)}-Re_{(2)}$	158.3(3)	151.8
$Re_{(2)}-O_{(5)}$	1.661(6)	1.678			$O_{(5)}-Re_{(2)}-O_{(4)}$	100.2(3)	103.2
$Re_{(2)}-F_{(2)}$	2.174(5)	2.243			$O_{(5)}-Re_{(2)}-F_{(5)}$	98.7(3)	99.0
$Re_{(2)}-F_{(7)}$	1.815(5)	1.888			$O_{(5)}-Re_{(2)}-F_{(6)}$	98.4(3)	98.6
$Re_{(2)}-F_{(5)}$	1.863(5)	1.859			$O_{(5)}-Re_{(2)}-F_{(7)}$	99.2(3)	98.1
$Re_{(2)}-F_{(6)}$	1.883(5)	1.941			$O_{(5)}-Re_{(2)}-F_{(2)}$	177.6(3)	174.0
Bond Angles (deg)					$O_{(4)}-Re_{(2)}-F_{(2)}$	82.0(2)	82.7
$O_{(1)}-Xe_{(1)}-O_{(1A)}$	180.0	180.0	180.0	180.0	$O_{(4)}-Re_{(2)}-F_{(5)}$	91.6(3)	95.9
$Xe_{(1)}-O_{(1)}-Xe_{(2)}$	115.6(3)	118.7	123.6	118.1	$O_{(4)}-Re_{(2)}-F_{(6)}$	161.2(3)	158.1
$O_{(1)}-Xe_{(2)}\cdots F_{(1)}$	176.7(2)	175.3		177.1	$O_{(4)}-Re_{(2)}-F_{(7)}$	94.3(3)	93.9
$Xe_{(2)}\cdots F_{(1)}-Re_{(1)}$	134.8(2)	130.7			$F_{(5)}-Re_{(2)}-F_{(2)}$	80.3(2)	81.0
$O_{(3)}-Re_{(1)}-O_{(2)}$	101.6(3)	102.8			$F_{(5)}-Re_{(2)}-F_{(6)}$	83.2(3)	83.2
$O_{(3)}-Re_{(1)}-F_{(1)}$	90.7(3)	88.9			$F_{(5)}-Re_{(2)}-F_{(7)}$	159.8(3)	157.8
$O_{(3)}-Re_{(1)}-F_{(2)}$	168.1(3)	165.5			$F_{(2)}-Re_{(2)}-F_{(6)}$	79.3(2)	75.5
$O_{(3)}-Re_{(1)}-F_{(3)}$	96.3(3)	97.1			$F_{(2)}-Re_{(2)}-F_{(7)}$	81.4(2)	80.6
$O_{(3)}-Re_{(1)}-F_{(4)}$	97.6(3)	97.4			$F_{(6)}-Re_{(2)}-F_{(7)}$	85.1(3)	80.3
$O_{(2)}-Re_{(1)}-F_{(1)}$	167.7(2)	168.3			$O_{(5)}-Re_{(2)}-F_{(6)}$	98.4(3)	98.6
$O_{(2)}-Re_{(1)}-F_{(2)}$	90.2(2)	91.6			$O_{(5)}-Re_{(2)}-F_{(7)}$	99.2(3)	98.1
$O_{(2)}-Re_{(1)}-F_{(3)}$	96.4(2)	97.8			$O_{(5)}-Re_{(2)}-F_{(2)}$	177.6(3)	174.0
$O_{(2)}-Re_{(1)}-F_{(4)}$	96.4(3)	97.8			$O_{(4)}-Re_{(2)}-F_{(2)}$	82.0(2)	82.7
$F_{(1)}-Re_{(1)}-F_{(2)}$	77.5(2)	76.7			$O_{(4)}-Re_{(2)}-F_{(5)}$	91.6(3)	95.9
$F_{(1)}-Re_{(1)}-F_{(3)}$	82.4(2)	80.4			$O_{(4)}-Re_{(2)}-F_{(6)}$	161.2(3)	158.1
$F_{(1)}-Re_{(1)}-F_{(4)}$	81.5(2)	80.5			$O_{(4)}-Re_{(2)}-F_{(7)}$	94.3(3)	93.9
$F_{(2)}-Re_{(1)}-F_{(3)}$	80.5(2)	80.5			$F_{(5)}-Re_{(2)}-F_{(2)}$	80.3(2)	81.0
$F_{(2)}-Re_{(1)}-F_{(4)}$	82.7(2)	80.6			$F_{(5)}-Re_{(2)}-F_{(6)}$	83.2(3)	83.2
$F_{(3)}-Re_{(1)}-F_{(4)}$	158.8(2)	155.8			$F_{(5)}-Re_{(2)}-F_{(7)}$	159.8(3)	157.8
$Re_{(1)}-F_{(2)}-Re_{(2)}$	158.3(3)	151.8			$F_{(2)}-Re_{(2)}-F_{(6)}$	79.3(2)	75.5
$O_{(5)}-Re_{(2)}-O_{(4)}$	100.2(3)	103.2			$F_{(2)}-Re_{(2)}-F_{(7)}$	81.4(2)	80.6
$O_{(5)}-Re_{(2)}-F_{(5)}$	98.7(3)	99.0			$F_{(6)}-Re_{(2)}-F_{(7)}$	85.1(3)	80.3

[a]See Figure 1 for the atom labeling scheme. [b]The B3LYP/aug-cc-pVDZ(-PP) level of theory was used. For values at the PBE1PBE/aug-cc-pVDZ(-PP) level of theory, see Table S1.

($Xe_{(1)}$) and 1.57 ($Xe_{(2,2A)}$) (Table S2). The introduction of the aforementioned long contacts results in total bond valences of 1.84 ($Xe_{(1)}$) and 1.81 ($Xe_{(2,2A)}$). The next closest Xe···O and Xe···F distances have bond valences <0.01 and are too long to be considered as contacts.

The central xenon atom of $[XeOXeOXe]^{2+}$ is located on an inversion center, whereas all other atoms of the cation and anion are on general positions, giving C_i symmetry for the ion pair. The $[XeOXeOXe]^{2+}$ cation is planar by symmetry and, when considered in isolation, has C_{2h} symmetry. The central $Xe_{(1)}-O_{(1,1A)}$ bonds (2.135(6) Å) are significantly longer and more polar than the terminal $Xe_{(2,2A)}-O_{(1,1A)}$ bonds (1.987(6) Å), in accordance with the dominant resonance contributions, (**1**) and (**2**).

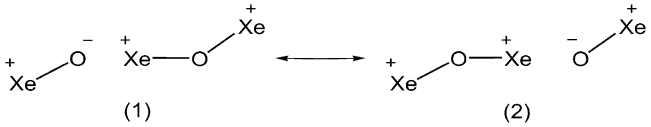

The central $Xe_{(1)}-O_{(1,1A)}$ bond lengths are equal, within $\pm3\sigma$, to the Xe–O bond lengths of $Xe(OTeF_5)_2$ (2.119(11) Å),[46] $FXeOSO_2F$ (2.155(8) Å),[47] $Xe(OSO_2F)_2$ (2.1101(13), 2.1225(13) Å),[48] and $FXeONO_2$ (2.126(4) Å).[49] The terminal $Xe_{(2,2A)}-O_{(1,1A)}$ bond lengths are equal, within $\pm3\sigma$, to the Xe–O bond lengths of $[XeOTeF_5][Sb(OTeF_5)_6]\cdot SO_2ClF$ (1.969(4) Å).[50] The $Xe_{(2,2A)}-O_{(1,1A)}$ bonds are slightly shorter than the Xe–O bonds of $Xe(OTeF_5)_2$,[46] $Xe(OTeF_5)_4$ (2.039(5), 2.026(5) Å),[51] and $O_2Xe(OTeF_5)_2$ (2.024(5),

DOI: 10.1021/jacs.5b08765
J. Am. Chem. Soc. 2015, 137, 13398–13413

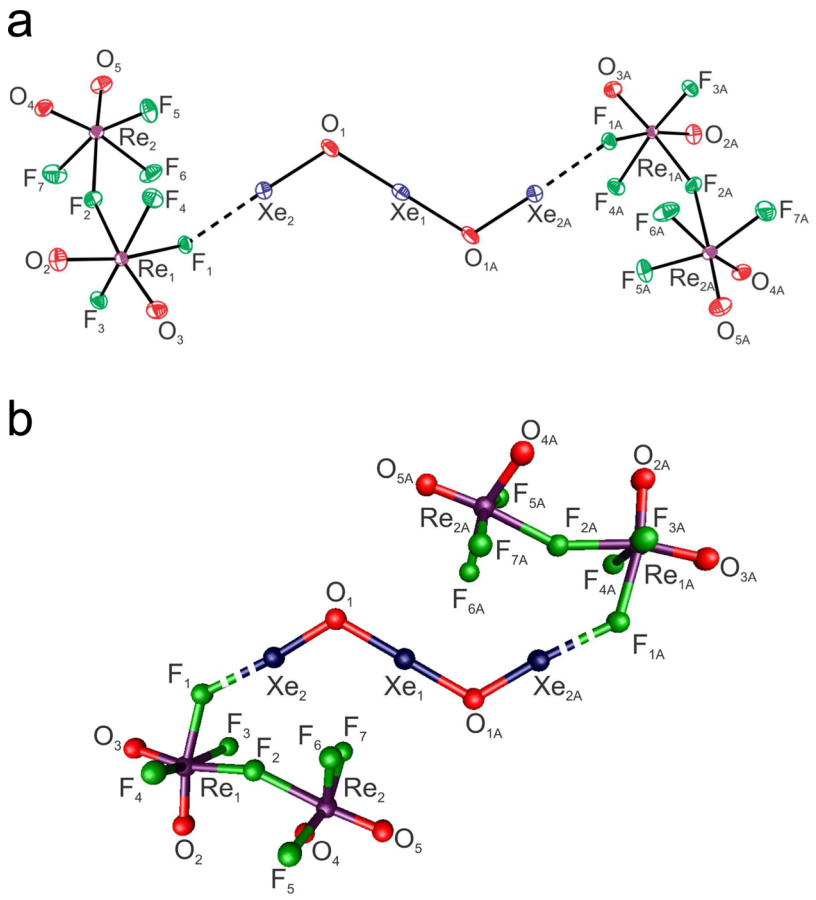

Figure 1. (a) The crystal structure of $[XeOXeOXe][\mu\text{-}F(ReO_2F_3)_2]_2$. Thermal ellipsoids are shown at the 50% probability level. (b) Calculated gas-phase structure of $[XeOXeOXe][\mu\text{-}F(ReO_2F_3)_2]_2$ (B3LYP/aug-cc-pVDZ(-PP)). The experimental and calculated geometric parameters are provided in Tables 2 and S1.

2.020(4) Å),[51] but are significantly shorter than the Xe−O bonds of $FXeOSO_2F$[47] and $FXeONO_2$.[49]

The $Xe_{(2,2A)}$---$F_{(1,1A)}$ bridge bonds between the $[XeOXeOXe]^{2+}$ cation and the $[\mu\text{-}F(ReO_2F_3)_2]^-$ anions (2.392(4) Å) are considerably longer and more polar than the terminal Xe−F bonds of XeF_2 (1.999(4) Å).[52] Overall, the $Xe_{(2,2A)}$---$F_{(1,1A)}$ cation−anion bridge bonds are slightly longer than the Xe---F bridge bonds in a number of $[XeF]^+$ salts, e.g., $[XeF][AsF_6]$ (2.208(3),[52] 2.212(5) Å),[53] $[XeF][SbF_6]$ (2.278(2) Å),[52] $[XeF][BiF_6]$ (2.204(7) Å),[52] $[XeF][Sb_2F_{11}]$ (2.343(4) Å),[52] and $[XeF][Bi_2F_{11}]$ (2.253(5) Å),[52] consistent with the dominant electrostatic nature of the $Xe_{(2,2A)}$---$F_{(1,1A)}$ interaction in $[XeOXeOXe][\mu\text{-}F(ReO_2F_3)_2]_2$ (also see Computational Results).

The $O_{(1)}$−$Xe_{(1)}$−$O_{(1A)}$ bond angle is linear by symmetry, whereas the $O_{(1,1A)}$−$Xe_{(2,2A)}$---$F_{(1,1A)}$ bridge bond angles slightly deviate from linearity (176.7(2)°). Both bond angles are consistent with linear AX_2E_3 VSEPR arrangements[54] in which three valence electron lone pairs of xenon occupy equatorial positions and two bonding electron pairs occupy axial positions. Similar near-linear fluorine bridge angles occur for $F-Xe^{II}$---F and $O-Xe^{II}$---F in $[FXeOXeFXeF][PnF_6]$ (As, 177.4(5)°, 178.3(5)°, 178.2(5)°; Sb, 178.6(3)°, 177.9(1)°),[39] $[XeF][AsF_6]$ (179.1(2)°,[52] 178.9(7)°),[53] $[XeF][SbF_6]$ (177.94(9)°),[52] $[XeF][BiF_6]$ (178.4(3)°),[52] $[XeF][Sb_2F_{11}]$ (179.3(2)°),[52] $[XeF][Bi_2F_{11}]$ (178.9(3)°),[52] and $FXeOSO_2F$ (177.4(3)°).[47]

The bent $Xe_{(1)}$−$O_{(1,1A)}$−$Xe_{(2,2A)}$ (115.6(3)°) and $Xe_{(2,2A)}$---$F_{(1,1A)}$−$Re_{(1,1A)}$ (134.8(2)°) bond angles are in accordance with AX_2E_2 VSEPR arrangements at the oxygen and fluorine atoms.[54] The $Xe_{(1)}$−$O_{(1,1A)}$−$Xe_{(2,2A)}$ bond angles are slightly smaller than the Xe−O−Ch (Ch = S, Se, or Te) angles in $Xe(OTeF_5)_2$ (121.2(6)°, 122.3(5)°),[46] $Xe(OSO_2F)_2$ (119.74(7), 119.18(7)°),[48] $FXeOSO_2F$ (123.7(5)°),[47] $Xe(OSeF_5)_2$ (123.9(13)°)[46] and are also less than the $Xe_{(1)}$−$O_{(1)}/F_{(1)}$−$Xe_{(2)}$ bond angle in $[FXeOXeFXeF][PnF_6]$ (As, 123.5(6)°, 123.6(6)°; Sb, 2 × 124.6(3)°).[39] The $Xe_{(2,2A)}$---$F_{(1,1A)}$−$Re_{(1,1A)}$ angles and related fluorine bridge angles are expected to be more open than the $Xe_{(1)}$−$O_{(1,1A)}$−$Xe_{(2,2A)}$ angle owing to reduced lone-pair—bond-pair repulsions between the bridge bonds and the electron lone pairs of the bridging fluorine atoms. The fluorine bridge angles that occur between the $[XeF]^+$ cation and its anion in $[XeF]^+$ salts are more open, e.g., $[XeF][AsF_6]$ (133.6(2)°,[52] 134.8(2)°),[53] $[XeF][SbF_6]$ (136.9(1)°),[52] $[XeF][BiF_6]$ (156.1(4)°),[52] $[XeF][Sb_2F_{11}]$ (148.1(2)°),[52] and $[XeF][Bi_2F_{11}]$ (151.3(3)°.[52]

The $[XeOXeOXe]^{2+}$ cation bridges to two $[\mu\text{-}F(ReO_2F_3)_2]^-$ anions through fluorine atoms that are trans to oxygen atoms of the anions. The preference for *trans*- versus *cis*-coordination is attributed to the trans influence of the doubly bonded oxygen atoms.[55] The bridging fluorine atom is a weaker $p_\pi \rightarrow d_\pi$ donor than the doubly bonded oxygen atom, therefore, more effective competition of the oxygen atom for the same two $d_{t_{2g}}$ orbitals of rhenium enhances the negative charge and basicity of the fluorine atom trans to it. In contrast, the terminal fluorine

DOI: 10.1021/jacs.5b08765
J. Am. Chem. Soc. 2015, 137, 13398−13413

atoms cis to the oxygen atom and trans to each other are less basic and, therefore, less favorable for fluorine bridge formation. Such *trans*-oxo fluorine bridges are found in other transition-metal oxide fluorides: $(ReO_2F_3)_\infty$,[41,56] $(TcO_2F_3)_\infty$,[55] $(OsO_3F_2)_\infty$,[57] $[\mu\text{-}F(TcOF_4)_2][Sb_2F_{11}]$,[58] $[\mu\text{-}F(ReOF_4)_2][Sb_2F_{11}]$,[59] $[\mu\text{-}F(OsO_2F_3)_2][Sb_2F_{11}]$,[60] and $[XeF_5][\mu\text{-}F(OsO_3F_2)_2]$.[61]

The $[\mu\text{-}F(ReO_2F_3)_2]^-$ anions of $K[\mu\text{-}F(ReO_2F_3)_2]$[41] and $K[\mu\text{-}F(ReO_2F_3)_2]\cdot 2ReO_2F_3$[41] have been structurally characterized by X-ray crystallography. Both salts display cation−anion interactions that are essentially Coulombic in nature. In contrast, the $[\mu\text{-}F(ReO_2F_3)_2]^-$ anions of $[XeOXeOXe][\mu\text{-}F(ReO_2F_3)_2]_2$ interact with the $[XeOXeOXe]^{2+}$ cation by means of fluorine bridges that lower the anion symmetries from C_{2v} to C_1. Despite a conformational change and symmetry lowering, the structural parameters and trends among the $[\mu\text{-}F(ReO_2F_3)_2]^-$ anion bond lengths and bond angles of the $[XeOXeOXe]^{2+}$ salt are comparable to those reported for $K[\mu\text{-}F(ReO_2F_3)_2]$ and $K[\mu\text{-}F(ReO_2F_3)_2]\cdot 2ReO_2F_3$, and are not further discussed.

In contrast with $K[\mu\text{-}F(ReO_2F_3)_2]$ and $K[\mu\text{-}F(ReO_2F_3)_2]\cdot 2ReO_2F_3$, where the Re−F−Re bridge bonds are equal by symmetry, the $Re_{(1,1A)}\text{−}F_{(2,2A)}\text{−}Re_{(2,2A)}$ bridge bonds of $[XeOXeOXe][\mu\text{-}F(ReO_2F_3)_2]_2$ are asymmetric. The fluorine bridge asymmetry is, to a large extent, indicative of the strength of the Xe---F bridging interactions between $[XeOXeOXe]^{2+}$ and $[\mu\text{-}F(ReO_2F_3)_2]^-$, showing shorter $Re_{(1,1A)}\text{−}F_{(2,2A)}$ bridge bonds that are proximate to the cation−anion bridges ($Re_{(1,1A)}\text{−}F_{(2,2A)}$, 2.048(4); $Re_{(2,2A)}\text{−}F_{(2,2A)}$, 2.174(5) Å). Similar asymmetries are found for the anions of $[XeF][Pn_2F_{11}]$ (Pn = Sb, Bi),[52] where the Pn−F−Pn bridge asymmetry is more pronounced in $[XeF][Bi_2F_{11}]$ (2.092(6), 2.195(6) Å) than in $[XeF][Sb_2F_{11}]$ (2.010(3), 2.066(3) Å) and is attributed to the greater ionic character of $[XeF][Sb_2F_{11}]$ and its weaker Xe---F bridge bond (Xe---F_{Sb}, 2.343(4) Å; Xe---F_{Bi}, 2.253(5) Å).[52]

Raman Spectroscopy. The low-temperature Raman spectra of $[Xe^{16/18}OXe^{16/18}OXe][\mu\text{-}F(Re^{16/18}O_2F_3)_2]_2$ are shown in Figure 2. The observed and calculated frequencies and mode descriptions are provided in Tables 3, S3, and S4. Spectral assignments were made by comparison with the calculated frequencies and Raman intensities of $[Xe^{16/18}OXe^{16/18}OXe][\mu\text{-}F(Re^{16/18}O_2F_3)_2]_2$ (C_i), $[Xe^{16/18}OXe^{16/18}OXe]^{2+}$ (C_{2h}) (Tables 3 and S5), and $[\mu\text{-}F(Re^{16/18}O_2F_3)_2]^-$ (C_1) (Table S6), which were optimized at the PBE1PBE/aug-cc-pVDZ(-PP) (values given in square brackets) and B3LYP/aug-cc-pVDZ(-PP) levels of theory. The vibrational modes of $[\mu\text{-}F(ReO_2F_3)_2]^-$, which had been previously assigned with the aid of LDFT and NLDFT calculations,[41] have been improved in the present work and are provided in Table S6, but are not further discussed.

The centrosymmetric, zigzag-shaped $[XeOXeOXe]^{2+}$ gas-phase cation possesses C_{2h} symmetry. Its nine fundamental vibrational modes span the irreducible representations $\Gamma = 3A_g + 2A_u + 4B_u$, where the A_u and B_u modes are infrared active and only the A_g modes are Raman active. The $\nu_1(A_g)$ band, corresponding to the symmetric out-of-phase $[\nu(Xe_1O_1) + \nu(Xe_{1A}O_{1A})] - [\nu(Xe_2O_1) + \nu(Xe_2O_{1A})]$ stretching mode, occurs at 581.6 cm^{-1} and exhibits a ^{18}O isotope shift of −32.3 cm^{-1}. The most intense band in the Raman spectrum occurs at 358.7 cm^{-1} with a ^{18}O isotope shift of −17.8 cm^{-1} and is assigned to $\nu_2(A_g)$. This band corresponds to $[\nu(Xe_1O_1) + \nu(Xe_1O_{1A})] + [\nu(Xe_2O_1) + \nu(Xe_{2A}O_{1A})]$ and is the in-phase counterpart of $\nu_1(A_g)$. The $\nu_3(A_g)$ band, corresponding to the symmetric in-phase $[\delta(Xe_2O_1Xe_1) + \delta(Xe_{2A}O_{1A}Xe_1)]_{i.p.}$ bending mode, occurs at 92.8 cm^{-1} with a ^{18}O isotope shift of −2.5 cm^{-1}.

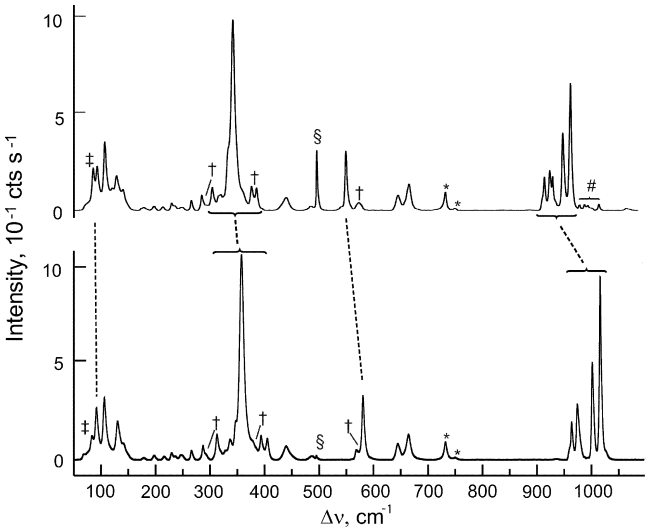

Figure 2. Raman spectra of $[XeOXeOXe][\mu\text{-}F(ReO_2F_3)_2]_2$ recorded at −140 °C using 1064 nm excitation for natural abundance (lower trace) and ∼97% ^{18}O-enriched (upper trace). Symbols denote FEP sample tube lines (*), instrumental artifact (‡), overlap of $[XeOXeOXe][\mu\text{-}F(ReO_2F_3)_2]_2$ lines with FEP sample tube lines (†), unreacted XeF_2 (§), and small quantities of ^{16}O and mixed $^{16/18}O$ isotopomers of the $[\mu\text{-}F(ReO_2F_3)_2]^-$ anion (#).

The calculated gas-phase $^{16/18}O$ isotopic shifts of the free $[XeOXeOXe]^{2+}$ cation are in good agreement with their experimental values ($\nu_1(A_g)$, −29.7 [−32.2] cm^{-1}; $\nu_2(A_g)$, −18.1 [−19.5] cm^{-1}; $\nu_3(A_g)$, −0.4 [−0.3] cm^{-1}). There is also good agreement between the experimental and calculated frequencies of the free $[XeOXeOXe]^{2+}$ cation for $\nu_1(A_g)$ (565.3 [611.3] cm^{-1}) and $\nu_2(A_g)$ (326.1 [353.6] cm^{-1}); however, the calculated frequency of $\nu_3(A_g)$ is underestimated (71.3 [74.9] cm^{-1}) by both methods. Optimization of the $[XeOXeOXe][\mu\text{-}F(ReO_2F_3)_2]_2$ ion pair resulted in similar $^{16/18}O$ isotopic shifts ($\nu_1(A_g)$, −29.8 [−32.5] cm^{-1}; $\nu_2(A_g)$, −18.9 [−17.3] cm^{-1}; $\nu_3(A_g)$, −0.3 [−0.3] cm^{-1}) and in slightly higher vibrational frequencies ($\nu_1(A_g)$, 580.1 [621.8] cm^{-1}; $\nu_2(A_g)$, 376.2 [397.4] cm^{-1}; $\nu_3(A_g)$, 89.9 [94.4] cm^{-1}) that are in better agreement with the experimental values. None of the symmetric modes of the cation are coupled to anion modes in the ion pair.

The frequency and isotopic shift of $[\nu(Xe_1O_1) + \nu(Xe_{1A}O_{1A})] - [\nu(Xe_2O_1) + \nu(Xe_2O_{1A})]$ are comparable to those of the antisymmetric $[\nu(Xe_1O_1) - \nu(Xe_2O_1)]$ stretching mode of $[FXeOXeFXeF]^+$ (595.8 cm^{-1}; $\Delta\nu^{16/18}$, −27.0 and −31.4 cm^{-1}).[39] The corresponding symmetric mode of $[FXeOXeFXeF]^+$ was coupled to Xe−F stretches and consequently occurred at higher frequency than that of $[XeOXeOXe][\mu\text{-}F(ReO_2F_3)_2]_2$ (418.7 and 429.8 cm^{-1}; $\Delta\nu^{16/18}$, −24.8 and −27.8 cm^{-1}, respectively). The anion bands have been fully assigned (Table S3 and S4) and are in good agreement with those of $K[\mu\text{-}F(ReO_2F_3)_2]$,[41] $K[\mu\text{-}F(ReO_2F_3)_2]\cdot 2ReO_2F_3$,[41] and $ReO_3F\cdot 2HF$.[40]

Computational Results. Quantum-chemical calculations for $[Xe^{16/18}OXe^{16/18}OXe][\mu\text{-}F(Re^{16/18}O_2F_3)_2]_2$ (C_i) and $[Xe^{16/18}OXe^{16/18}OXe]^{2+}$ (C_{2h}) were carried out using the PBE1PBE (values in square brackets) and B3LYP methods and the aug-cc-pVDZ(-PP) basis set. Although the optimiza-

DOI: 10.1021/jacs.5b08765
J. Am. Chem. Soc. 2015, 137, 13398−13413

Table 3. Selected Experimental and Calculated Vibrational Frequencies, $^{16/18}$O Isotopic Shifts ($\Delta\nu^{16/18}$), and Assignments[a] for $[XeOXeOXe]^{2+}$ in $[XeOXeOXe][\mu\text{-}F(ReO_2F_3)_2]_2$ and Gas-Phase $[XeOXeOXe]^{2+}$

$[Xe^{16/18}OXe^{16/18}OXe][\mu\text{-}F(Re^{16/18}O_2F_3)_2]_2$						$[Xe^{16/18}OXe^{16/18}OXe]^{2+}$				
exptl[b]			calcd (C_i)[c]			calcd (C_{2h})[c]				
^{16}O	^{18}O	$\Delta\nu^{16/18}$	^{16}O	^{18}O	$\Delta\nu^{16/18}$	^{16}O	^{18}O	$\Delta\nu^{16/18}$	assgnts[d]	
581.6(31)	549.3(30)	−32.3	580.1(110)[0]	550.3(94)[0]	−29.8	565.3(20)[0]	535.6(17)[0]	−29.7	$\nu_1(A_g)$	$[\nu(Xe_1O_1) + \nu(Xe_1O_{1A})] - [\nu(Xe_2O_1) + \nu(Xe_{2A}O_{1A})]$
			565.0(0)[322]	535.6(0)[304]	−29.4	548.0(0)[18]	519.5(0)[16]	−28.5	$\nu_4(B_u)$	$[\nu(Xe_1O_1) - \nu(Xe_1O_{1A})] - [\nu(Xe_2O_1) - \nu(Xe_{2A}O_{1A})]$
			465.5(0)[201][e]	440.1(0)[165][e]	−25.4	407.1(0)[90]	387.4(0)[83]	−19.7	$\nu_5(B_u)$	$[\nu(Xe_1O_1) - \nu(Xe_1O_{1A})] + [\nu(Xe_2O_1) - \nu(Xe_{2A}O_{1A})]$
358.7(100)	340.9(100)	−17.8	376.2(139)[0]	357.3(125)[0]	−18.9	326.1(30)[0]	308.0(27)[0]	−18.1	$\nu_2(A_g)$	$[\nu(Xe_1O_1) + \nu(Xe_1O_{1A})] + [\nu(Xe_2O_1) + \nu(Xe_{2A}O_{1A})]$
			173.4(0)[8][f]	172.7(0)[7][f]	−0.7	160.3(0)[4]	159.9(0)[4]	−0.4	$\nu_6(B_u)$	$[\delta(Xe_2O_1Xe_1) - \delta(Xe_{2A}O_{1A}Xe_1)]_{i.p.}$
			169.7(0)[4]	162.4(0)[4]	−7.3	115.0(0)[6]	110.4(0)[6]	−4.6	$\nu_8(A_u)$	$[\delta(Xe_2O_1Xe_1) - \delta(Xe_{2A}O_{1A}Xe_1)]_{o.o.p.}$
92.8(25)	90.3(23)	−2.5	89.9(24)[0]	89.6(24)[0]	−0.3	71.3(35)[0]	70.9(35)[0]	−0.4	$\nu_3(A_g)$	$[\delta(Xe_2O_1Xe_1) + \delta(Xe_{2A}O_{1A}Xe_1)]_{i.p.}$
			87.0(0)[9][g]	86.6(0)[9][g]	−0.4	34.5(0)[<1]	34.3(0)[<1]	−0.2	$\nu_7(B_u)$	$[\rho_r(Xe_2O_1Xe_1) - \rho_r(Xe_{2A}O_{1A}Xe_1)]$
						11.3(0)[3]	11.2(0)[3]	−0.1	$\nu_9(A_u)$	$[\rho_t(Xe_2O_1Xe_1) - \rho_t(Xe_{2A}O_{1A}Xe_1)]$

[a]A full list of frequencies and assignments is provided in Table S3. Vibrational frequencies and isotopic shifts are given in cm^{-1}; $\Delta\nu^{16/18} = \nu(^{18}O) - \nu(^{16}O)$. [b]The Raman spectrum was recorded in an FEP sample tube at −140 °C using 1064-nm excitation. Values in parentheses denote relative experimental Raman intensities. [c]B3LYP/aug-cc-pVDZ(-PP); the PBE1PBE values are given in Table S4. Values in parentheses denote calculated Raman intensities ($Å^4$ amu^{-1}). Values in square brackets denote calculated infrared intensities (km mol^{-1}). [d]Bond elongations and angle openings are denoted by plus (+) signs, and bond contractions and angle compressions are denoted by minus (−) signs. Abbreviations denote stretch (ν), bend (δ), rock (ρ_r), twist (ρ_t), in-plane (i.p.), and out-of-plane (o.o.p.). The atom labeling scheme is given in Figure 1. [e]There is also a small contribution from $[\nu(Xe_2F_1) - \nu(Re_1F_1)] + [\nu(Re_1F_2) - \nu(Re_2F_2)] + [\nu(Xe_{2A}F_{1A}) - \nu(Re_{1A}F_{1A})] - [\nu(Re_{1A}F_{2A}) - \nu(Re_{2A}F_{2A})]$ for this mode in the ion pair. [f]There is also a contribution from $[\rho_t(F_7Re_2F_6) - \rho_t(F_{7A}Re_{2A}F_{6A})]$ for this mode in the ion pair. [g]There is also a small contribution from $[\rho_r(Re_2O_4O_5F_5F_6F_7) - \rho_r(Re_{2A}O_{4A}O_{5A}F_{5A}F_{6A}F_{7A})]$ to this mode in the ion pair (Table S3).

J. Am. Chem. Soc. 2015, 137, 13398−13413
DOI: 10.1021/jacs.5b08765

Table 4. Natural Population Analysis Charges, Natural Atomic Orbital Bond Orders, and Valences for $[XeOXeOXe][\mu\text{-}F(ReO_2F_3)_2]_2$ (C_i), $[XeOXeOXe]^{2+}$ (C_{2h}), and FXeOXeOXeF (C_i)[a]

	$[XeOXeOXe][\mu\text{-}F(ReO_2F_3)_2]_2$	$[XeOXeOXe]^{2+}$	FXeOXeOXeF
Atom		Atomic Charge [Valence]	
$Xe_{(1)}$	1.061 [0.656]	1.084 [0.636]	0.966 [0.692]
$Xe_{(2)}$	1.095 [0.600]	1.095 [0.484]	1.044 [0.660]
$O_{(1)}$	−0.792 [0.786]	−0.638 [0.808]	−0.911 [0.741]
$F_{(1)}$	−0.621 [0.443]		−0.616 [0.260]
Bond		Bond Order	
$Xe_{(1)}-O_{(1)}$	0.330	0.321	0.342
$Xe_{(2)}-O_{(1)}$	0.461	0.486	0.395
$Xe_{(2)}-F_{(1)}$	0.141		0.259

[a]The B3LYP/aug-cc-pVDZ(-PP) basis set was used.

tions of $[Xe^{16/18}OXe^{16/18}OXe]^{2+}$ (C_{2h}) resulted in stationary points with all frequencies real (Tables 3 and S5; Figure S3), the optimizations of $[Xe^{16/18}OXe^{16/18}OXe][\mu\text{-}F(Re^{16/18}O_2F_3)_2]_2$ (C_i) (Tables 3, S3, and S4; Figure 1) each gave one imaginary frequency. Attempts to follow the imaginary frequencies resulted in conformers that were severely twisted about their $Xe_{(2,2A)}$---$F_{(1,1A)}$ bridge bonds; thus, all subsequent NBO, QTAIM, ELF, and MEPS calculations were carried out using the calculated C_i geometry. The hypothetical $FXe^{16/18}OXe^{16/18}OXeF$ (C_{2h}) molecule was also calculated in order to better assess the nature of the Xe---F bridge bonds in the ion pair (Tables 3 and S7; Figure S3). The $[\mu\text{-}F(ReO_2F_3)_2]^-$ anion was also calculated to aid with the anion mode assignments of the ion pair (Table S6; Figure S3).

Geometry Optimizations. The calculated symmetry of the ion pair is C_i and the local symmetry of the $[XeOXeOXe]^{2+}$ cation is C_{2h}. The local gas-phase symmetry of $[XeOXeOXe]^{2+}$ is the same as in the crystal structure. Although the calculated gas-phase ion pair and the solid-state ion pair have the same point group symmetry, their conformations differ. In the calculated ion-pair, the Xe and Re atoms of both anions are coplanar, whereas the Re···F···Re axis in the solid-state structure is approximately perpendicular to the $Xe_{(2)}\cdots Xe_{(1)}\cdots Xe_{(2A)}$ axis (Figure 1). The calculated bond valences of $Xe_{(1)}$ and $Xe_{(2,2A)}$ (Table S2) suggest that the reorientation of the anions most likely stems from the need for each Xe atom to complete its valency requirement through additional long intramolecular Xe···F contacts. In the crystal structure, similar intermolecular Xe···F contacts occur between neighboring ion pairs (see X-ray Crystallography); however, in the calculated gas-phase ion pair, the xenon atoms can only achieve their valence complements through intramolecular contacts (Table S2), resulting in a conformation that substantially differs with respect to the crystallographic conformation.

Despite the conformational difference between the calculated and experimental ion pairs, all experimental bond length and bond angle trends were well reproduced by the quantum-chemical calculations (Tables 2 and S1). The central $Xe_{(1)}-O_{(1,1A)}$ bond lengths (calcd, 2.174 [2.139] Å; exptl, 2.135(6) Å) are longer than the terminal $Xe_{(2,2A)}-O_{(1,1A)}$ bond lengths (calcd, 2.034 [2.007] Å; exptl, 1.987(6) Å). The $O_{(1)}-Xe_{(1)}-O_{(1A)}$ angle is linear by symmetry, whereas the $Xe_{(1)}-O_{(1,1A)}-Xe_{(2,2A)}$ bond angles (calcd, 118.7 [118.0]°; exptl, 115.6(3)°) are significantly bent. The calculated $Xe_{(2)}$---$F_{(1,1A)}$ bridge bond lengths (2.310 [2.279] Å) are slightly overestimated compared to the experimental values (2.392(4) Å). The calculated $F_{(1,1A)}$---$Xe_{(2,2A)}-O_{(1,1A)}$ bond angles are also in very good agreement with experiment (calcd, 175.3 [175.2]°; exptl, 176.7(2)°). A comparison of the geometrical trends of the calculated ion pair with those of the free $[XeOXeOXe]^{2+}$ cation ($Xe_{(1)}-O_{(1,1A)}$, 2.207 [2.169] Å; $Xe_{(2,2A)}-O_{(1,1A)}$, 2.021 [1.994] Å; $Xe_{(1)}-O_{(1,1A)}-Xe_{(2,2A)}$, 123.6 [122.5]°) shows that the central $Xe_{(1)}-O_{(1,1A)}$ bond lengths and $Xe_{(1)}-O_{(1,1A)}-Xe_{(2,2A)}$ bond angles slightly decrease upon ion pair formation, but the terminal $Xe_{(2,2A)}-O_{(1,1A)}$ bond lengths remain essentially unchanged.

In order to assess the degree of ion pairing, the energy-minimized geometry of the hypothetical FXeOXeOXeF molecule was calculated. Although the O−Xe−O (180.0°), Xe−O−Xe (118.1 [117.0]°), and O−Xe−F (177.1 [177.4]°) bond angles are comparable to those of the ion pair, fluoride ion coordination affects the Xe−O bond lengths. The central $Xe_{(1)}-O_{(1,1A)}$ bond lengths are shorter (2.155 [2.119] Å), whereas the terminal $Xe_{(2,2A)}-O_{(1,1A)}$ bond lengths are longer (2.098 [2.068] Å) than those of $[XeOXeOXe]^{2+}$; however, the relative bond length order, $Xe_{(1)}-O_{(1,1A)} > Xe_{(2,2A)}-O_{(1,1A)}$ remains unchanged. The $Xe_{(2,2A)}-F_{(1,1A)}$ bond lengths (2.086 [2.057] Å) of FXeOXeOXeF are considerably shorter and more covalent than the $Xe_{(2,2A)}$---$F_{(1,1A)}$ bridge bonds (2.310 [2.279] Å) of the gas-phase ion pair, $[XeOXeOXe][\mu\text{-}F(ReO_2F_3)_2]_2$.

The geometrical parameters and trends within the $[\mu\text{-}F(ReO_2F_3)_2]^-$ anions (Re−O < Re−F < Re−F_μ; O−Re−O > O−Re−F > O−Re−F_μ > F−Re−F_μ) of the calculated ion pair are similar to those of the experimental structure (Tables 2 and S1).

Natural Bond Orbital (NBO) Analyses. The NBO analyses for the $[XeOXeOXe][\mu\text{-}F(ReO_2F_3)_2]_2$ ion pair (C_i), $[XeOXeOXe]^{2+}$ (C_{2h}), and FXeOXeOXeF (C_i) were carried out for the B3LYP/aug-cc-pVDZ(-PP) and PBE1PBE/aug-cc-pVDZ(-PP) optimized gas-phase geometries and are compared with those of the $[FXeOXeFXeF]^+$ cation.[39] The trends in calculated charges, valences, and bond orders for the above molecules are consistent at both levels of theory (Tables 4 and S8).

Overall, the $Xe_{(1)}$, $Xe_{(2,2A)}$, $O_{(1,1A)}$, and $F_{(1,1A)}$ charges of $[XeOXeOXe][\mu\text{-}F(ReO_2F_3)_2]_2$, $[XeOXeOXe]^{2+}$, and FXeOXeOXeF are nearly half of the formal charges expected for purely ionic interactions (Xe, +2; O, −2; F, −1) and are consistent with semi-ionic bonding. The $Xe_{(1)}$ and $Xe_{(2,2A)}$ charges of the free cation (+1.085 and +1.095, respectively), are in accordance with resonance structures (**1**) and (**2**) and do not change significantly when $[XeOXeOXe]^{2+}$ forms fluorine bridges with the $[\mu\text{-}F(ReO_2F_3)_2]^-$ anions of the ion pair (+1.061 and +1.095), but decrease significantly upon formation of the hypothetical FXeOXeOXeF molecule (+0.966 and +1.044). The O charges become more negative upon ion-pair

DOI: 10.1021/jacs.5b08765
J. Am. Chem. Soc. 2015, 137, 13398−13413

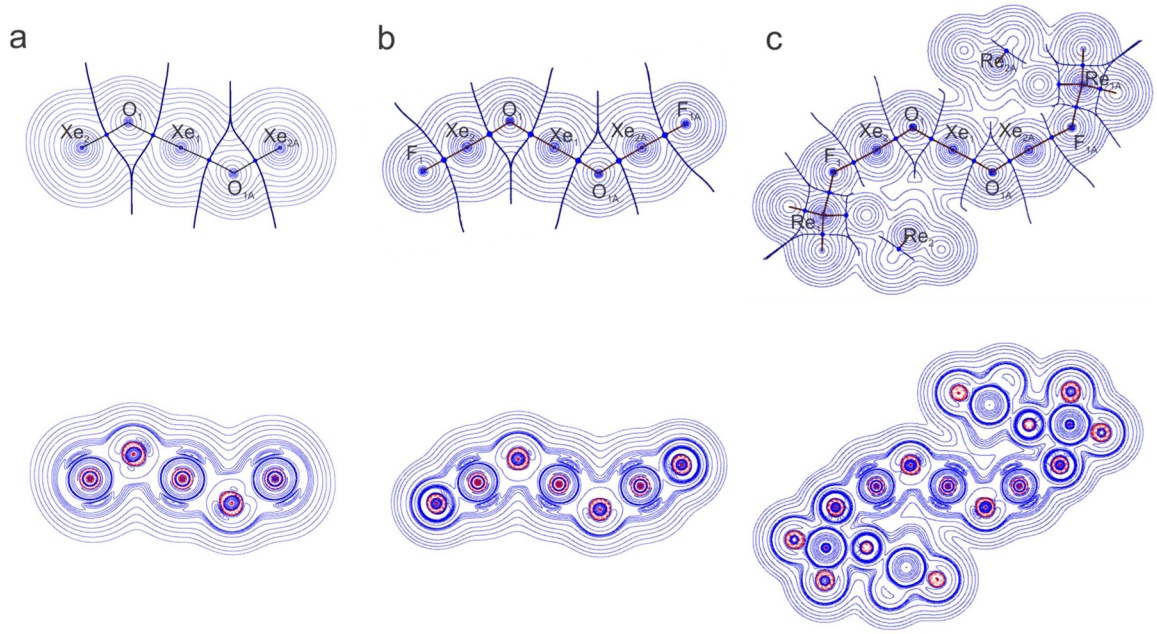

Figure 3. Contour maps of the charge density showing the bond paths and the intersection of the interatomic surfaces (top) and charge density contour maps of the Laplacian distribution (bottom) in (a) $[XeOXeOXe]^{2+}$, (b) FXeOXeOXeF, and (c) $[XeOXeOXe][\mu\text{-}F(ReO_2F_3)_2]_2$. The nuclear positions in the contour maps of the charge density are identical to those in the contour maps of the Laplacian distribution. The contour values start at ±0.001 au and increase in the order $\pm 2 \times 10^n$, $\pm 4 \times 10^n$, and $\pm 8 \times 10^n$ with n starting at −3 and increasing in steps of 1 to give a maximum contour value of 8×10^6 with several additional contour values on the contour maps of the Laplacian distribution (±0.05, ±0.06, ±0.07, ±0.5, ±0.55, ±0.6, ±0.65, ±0.7, ±0.75 au). Bond critical points are denoted by blue dots. Solid blue contours denote positive, and dashed red lines denote negative values of $\nabla^2\rho$.

formation ($[XeOXeOXe]^{2+}$, −0.638; $[XeOXeOXe][\mu\text{-}F(ReO_2F_3)_2]_2$, −0.792) and are most negative in the neutral FXeOXeOXeF molecule (−0.911). The $F_{(1,1A)}$ charges of the ion pair (−0.621) are similar to those of FXeOXeOXeF (−0.616). The positive charge transferred from the XeOXeOXe-moiety of the ion pair (+0.333) to its anions is considerably less than that transferred from the XeOXeOXe-moiety of FXeOXeOXeF (+0.768) to its F-ligands.

The $Xe_{(1)}$−$O_{(1,1A)}$ bond orders are comparable among the three species, ranging from 0.321 to 0.342. The $Xe_{(2,2A)}$−$O_{(1,1A)}$ bond orders are similar for free $[XeOXeOXe]^{2+}$ (0.486) and for the ion pair (0.461). In contrast, the $Xe_{(2,2A)}$−$O_{(1,1A)}$ bond orders of FXeOXeOXeF (0.395) are smaller, indicating that the $Xe_{(2,2A)}$−$O_{(1,1A)}$ bonds are less covalent than the $Xe_{(1)}$−$O_{(1,1A)}$ bonds. The $Xe_{(2,2A)}$---$F_{(1,1A)}$ bridge bond orders of the ion pair (0.141) are approximately half of the $Xe_{(2,2A)}$−$F_{(1,1A)}$ bond orders of FXeOXeOXeF (0.259), indicating significantly weaker covalent interactions for the $Xe_{(2,2A)}$---$F_{(1,1A)}$ bridge bonds of the ion pair than for the terminal $Xe_{(2,2A)}$−$F_{(1,1A)}$ bonds of FXeOXeOXeF.

The $Xe_{(1)}$ valences of the ion pair (0.656) and FXeOXeOXeF (0.692) are only slightly greater than that of the free cation (0.636), whereas the $Xe_{(2,2A)}$ valences increase significantly from $[XeOXeOXe]^{2+}$ (0.484) to the ion pair (0.600) and are highest in FXeOXeOXeF (0.660). The $O_{(1,1A)}$ valences of the ion pair (0.786) are comparable to those of the free cation (0.808) and slightly greater than the $O_{(1,1A)}$ valences of FXeOXeOXeF (0.741). The $F_{(1,1A)}$ atom valences are in accordance with the semi-ionic characters of the $Xe_{(2,2A)}$---$F_{(1,1A)}$ bonds in the ion pair (0.443) and FXeOXeOXeF (0.260). The higher valences of the bridging $F_{(1,1A)}$ atoms of the ion pair are in accordance with their higher coordination numbers.

QTAIM Analyses. The natures of the Xe−O and Xe−F bonds in the free $[XeOXeOXe]^{2+}$ cation, the $[XeOXeOXe][\mu\text{-}F(ReO_2F_3)_2]_2$ ion pair, and the hypothetical FXeOXeOXeF molecule have been investigated by complementary use of the quantum theory of atoms in molecules QTAIM[62] and the topological[63] analysis of the Becke and Edgecombe electron localization function (ELF).[64]

The contour maps of the charge densities showing the bond paths and intersections of atomic surfaces (Figure 3), charge density contour maps of the Laplacian distributions ($\nabla^2\rho$) (Figure 3), and valence shells of charge concentration (VSCC) relief maps ($-\nabla^2\rho$) (Figure S4) are provided for $[XeOXeOXe]^{2+}$, $[XeOXeOXe][\mu\text{-}F(ReO_2F_3)_2]_2$, and FXeOXeOXeF.

For two atoms to be bonded to one another, they must be linked by a bond path, indicating that some electronic charge is accumulated between the two nuclei. The presence of a bond path implies the existence of a bond critical point along it, where the charge density, ρ, is at its minimum value, but is a maximum with respect to lines perpendicular to its bond path.[62] The charge distributions (Figure 3) of the aforementioned species exhibit such bond paths between the Xe and O nuclei and between the Xe and F nuclei. Several AIM properties (Tables 5 and S9) evaluated at the bond critical points (denoted by subscripted b in the ensuing discussion and by blue dots in Figure 3) can be used to assess the nature of a bond.[62] For example, significantly negative values for the Laplacian of the electron density ($\nabla^2\rho_b$) and a density of all electrons (ρ_b) > 0.2 au are associated with covalent bonding. Significantly negative values for the total energy density of Cremer and Kraka (H_b) are also consistent with strong covalent bonds. The energy, H_b, is defined as the sum of G_b and V_b, where G_b is the Lagrangian kinetic energy and V_b is the

DOI: 10.1021/jacs.5b08765
J. Am. Chem. Soc. 2015, 137, 13398−13413

Table 5. QTAIM Density of all Electrons (ρ_b), Laplacian of Electron Density ($\nabla^2\rho_b$), Energy Density (H_b), QTAIM Delocalization Indices (δ), QTAIM Atomic Populations ($\bar{N}$), and ELF Basin Populations ($\bar{N}$) in $[XeOXeOXe]^{2+}$, FXeOXeOXeF, and $[XeOXeOXe]^{2+}$ in $[XeOXeOXe][\mu\text{-}F(ReO_2F_3)_2]_2$[a,b,c]

bond	ρ_b	$\nabla^2\rho_b$	H_b	δ	$\bar{N}$		$\bar{N}$[A]	
				$[XeOXeOXe]^{2+}$ in $[XeOXeOXe][\mu\text{-}F(ReO_2F_3)_2]_2$ (C_i)				
$Xe_{(1)}-O_{(1)}$	0.091	0.170	−0.023	0.81	$\bar{N}(Xe_{(1)})$	52.96	$\bar{N}[C(Xe_{(1)})]$[d]	46.34
$Xe_{(2)}-O_{(1)}$	0.123	0.161	−0.048	1.12	$\bar{N}(Xe_{(2)})$	52.92	$\bar{N}[V(Xe_{(1)})]$	7.15
$Xe_{(2)}\cdots F_{(1)}$	0.058	0.168	−0.008	0.43	$\bar{N}(O_{(1)})$	8.75	$\bar{N}[C(Xe_{(2)})]$[d]	46.34
					$\bar{N}(F_{(1)})$	9.68	$\bar{N}[V(Xe_{(2)})]$	7.02
							$\bar{N}[C(O_{(1)})]$	2.12
							$\bar{N}[V(O_{(1)})]$	6.78
							$\bar{N}[C(F_{(1)})]$	2.18
							$\bar{N}[V(F_{(1)})]$	7.57
				$[XeOXeOXe]^{2+}$ (C_{2h})				
$Xe_{(1)}-O_{(1)}$	0.084	0.162	−0.018	0.78	$\bar{N}(Xe_{(1)})$	52.94	$\bar{N}[C(Xe_{(1)})]$[d]	46.42
$Xe_{(2)}-O_{(1)}$	0.125	0.142	−0.049	1.26	$\bar{N}(Xe_{(2)})$	52.93	$\bar{N}[V(Xe_{(1)})]$	7.16
					$\bar{N}(O_{(1)})$	8.59	$\bar{N}[C(Xe_{(2)})]$[d]	46.42
							$\bar{N}[V(Xe_{(2)})]$	7.05
							$\bar{N}[C(O_{(1)})]$	2.12
							$\bar{N}[V(O_{(1)})]$	6. 62
				FXeOXeOXeF (C_i)				
$Xe_{(1)}-O_{(1)}$	0.096	0.171	−0.027	0.86	$\bar{N}(Xe_{(1)})$	53.09	$\bar{N}[C(Xe_{(1)})]$[e]	45.79
$Xe_{(2)}-O_{(1)}$	0.108	0.173	−0.036	0.97	$\bar{N}(Xe_{(2)})$	52.97	$\bar{N}[V(Xe_{(1)})]$	7.24
$Xe_{(2)}-F_{(1)}$	0.098	0.233	−0.028	0.77	$\bar{N}(O_{(1)})$	8.86	$\bar{N}[C(Xe_{(2)})]$[e]	45.79
					$\bar{N}(F_{(1)})$	9.63	$\bar{N}[V(Xe_{(2)})]$	7.10
							$\bar{N}[C(O_{(1)})]$	2.13
							$\bar{N}[V(O_{(1)})]$	6.85
							$\bar{N}[C(F_{(1)})]$	2.16
							$\bar{N}[V(F_{(1)})]$	7.46

[a]B3LYP/aug-cc-pVDZ(-PP). [b]The atomic unit (au) for $\nabla^2\rho_b$ is e/a_0^5 (1 au = 24.098 e Å^{-5}). The au for ρ_b is e/a_0^3 (1 au = 6.748 e Å^{-3}). The au for H is e^2/a_0^4 (1 au = E_h/a_0^3 = 6.748 E_h/Å^3). a_0 = Bohr radius = 0.52918 Å. e = charge on an electron. E_h = hartree = e^2/a_0. [c]For atom labeling see Figures 1 and S3. [d]$\bar{N}[C(Xe_{(1)})] = \bar{N}[C(Xe_{(2,2A)})] = {}^1/_3\{178 - (\bar{N}[C(O_{(1)})] + \bar{N}[C(O_{(1A)})] + \bar{N}[V(O_{(1)})] + \bar{N}[V(O_{(1A)})] + \bar{N}[V(Xe_{(1)})] + \bar{N}[V(Xe_{(2)})] + \bar{N}[V(Xe_{(2A)})])\}$. [e]$\bar{N}[C(Xe_{(1)})] = \bar{N}[C(Xe_{(2,2A)})] = {}^1/_3\{196 - (\bar{N}[C(O_{(1)})] + \bar{N}[C(O_{(1A)})] + \bar{N}[C(F_1)] + \bar{N}[C(F_{1A})] + \bar{N}[V(O_{(1)})] + \bar{N}[V(O_{(1A)})] + \bar{N}[V(F_{(1)})] + \bar{N}[V(F_{(1A)})] + \bar{N}[V(Xe_{(1)})] + \bar{N}[V(Xe_{(2)})] + \bar{N}[V(Xe_{(2A)})])\}$.

potential energy density. In covalent bonds, G_b is dominated by V_b, giving a negative value for H_b. When dealing with semi-ionic bonds such as encountered in the present study, the sign or the small absolute values of the above properties can be ambiguous, and it is necessary to look at the combined properties to characterize the nature of the bond. In the present case, the delocalization indices (δ) were also considered, where the delocalization index provides a quantitative measure of the number of electron pairs delocalized between two atomic spaces.

The Xe−O bond properties of $[XeOXeOXe]^{2+}$, $[XeOXeOXe][\mu\text{-}F(ReO_2F_3)_2]_2$, and FXeOXeOXeF are consistent with resonance structures (**1**) and (**2**) and with the NBO analyses (see above). The small ρ_b values ($Xe_{(1)}-O_{(1,1A)}$, 0.084−0.096 au; $Xe_{(2,2A)}-O_{(1,1A)}$, 0.108−0.125 au) and positive $\nabla^2\rho_b$ values ($Xe_{(1)}-O_{(1,1A)}$, 0.162−0.171 au; $Xe_{(2,2A)}-O_{(1,1A)}$, 0.142−0.173 au) are consistent with semi-ionic Xe−O bonds. This description is supported by small δ_{Xe-O} delocalization indices ($Xe_{(1)}-O_{(1,1A)}$, 0.78−0.86; $Xe_{(2,2A)}-O_{(1,1A)}$, 0.97−1.26). The delocalization indices of the terminal $Xe_{(2,2A)}-O_{(1,1A)}$ bonds are greater than those of the central $Xe_{(1)}-O_{(1,1A)}$ bonds and are consistent with the shorter, more covalent, $Xe_{(2,2A)}-O_{(1,1A)}$ bonds observed for $[XeOXeOXe]^{2+}$ in the crystal structure of $[XeOXeOXe][\mu\text{-}F(ReO_2F_3)_2]_2$ and those calculated for $[XeOXeOXe]^{2+}$, the $[XeOXeOXe][\mu\text{-}F(ReO_2F_3)_2]_2$ ion pair, and FXeOXeOXeF. In the case of FXeOXeOXeF, the gap between $\delta_{Xe(1)-O(1,1A)}$ and $\delta_{Xe(2,2A)-O(1,1A)}$ is smaller, in accordance with terminal and central semi-ionic Xe−O bonds that possess similar covalent characters. The very small negative values of the total energy densities, H_b ($Xe_{(1)}-O_{(1,1A)}$, −0.018 to −0.027 au; $Xe_{(2,2A)}-O_{(1,1A)}$, −0.036 to −0.049 au), are also in agreement with a semi-ionic description for the Xe−O bonds, where the more negative H_b values correspond to the shorter, more covalent terminal $Xe_{(2,2A)}-O_{(1,1A)}$ bonds of all three species.

The $Xe_{(2,2A)}\text{---}F_{(1,1A)}$ bond properties of $[XeOXeOXe][\mu\text{-}F(ReO_2F_3)_2]_2$ and FXeOXeOXeF (ρ_b, 0.058 and 0.098 au; $\nabla^2 r_b$, 0.168 and 0.233 au; $\delta_{Xe(2,2A)\text{---}F(1,1A)}$, 0.43 and 0.77 au; H_b, −0.008 and −0.028 au, respectively) show that the $Xe_{(2,2A)}\text{---}F_{(1,1A)}$ bridge bonds of $[XeOXeOXe][\mu\text{-}F(ReO_2F_3)_2]_2$ are considerably more ionic than the terminal $Xe_{(2,2A)}-F_{(1,1A)}$ bonds of FXeOXeOXeF. This is consistent with the ionic formulations that have been adopted for the gas-phase and solid-state ion pairs.

The Xe and O valence electron lone pair (VELP) charge densities are readily discernible on the contour maps of $\nabla^2\rho$ (Figure 3). The charge densities of the three Xe VELPS combine to form tori around each Xe atom (see ELF Analyses). The tori lie in planes that are perpendicular to the molecular planes of $[XeOXeOXe]^{2+}$, FXeOXeOXeF, and the XeOXeOXe-plane of $[XeOXeOXe][\mu\text{-}F(ReO_2F_3)_2]_2$ so that the plane of the charge density contour map depicted in Figure 3 passes through each torus to give two VELP charge concentrations on either side of each Xe core.

DOI: 10.1021/jacs.5b08765
J. Am. Chem. Soc. 2015, 137, 13398−13413

Although the $F_{(1,1A)}$ VELP charge densities exhibit essentially spherical distributions in FXeOXeOXeF and $[XeOXeOXe][\mu\text{-}F(ReO_2F_3)_2]_2$, the Laplacian contour plot of the electron density around $F_{(1,1A)}$ and $Xe_{(2,2A)}$ in FXeOXeOXeF differs slightly from that of the ion pair. The Laplacian distribution of the charge density in FXeOXeOXeF (Figure 3b) exhibits a contour line enclosing $F_{1,1A}$ and $Xe_{2,2A}$, whereas the contours of $F_{1,1A}$ and $Xe_{2,2A}$ are not joined in the plot of the Laplacian distribution in the ion pair (Figure 3c). This is in agreement with the more ionic characters of the $Xe_{(2,2A)}$---$F_{(1,1A)}$ bridge bonds relative to those of the terminal $Xe_{(2,2A)}-F_{(1,1A)}$ bonds in FXeOXeOXeF.

Maxima in the relief maps $(-\nabla^2\rho)$ of $[XeOXeOXe]^{2+}$, FXeOXeOXeF, and $[XeOXeOXe][\mu\text{-}F(ReO_2F_3)_2]_2$ (Figure S4) denote maxima in charge concentrations. When the inner spike at its nucleus is counted, the Xe atom exhibits five alternating regions of charge concentration and depletions corresponding to five quantum shells. The VSCCs are not strongly linked for the Xe−O, Xe−F, and Xe−F bonds. Rather, their charges are predominantly concentrated in their atomic basins with small, shared charge concentrations. The Xe and O VELP densities are considerably more diffuse and less apparent in the VSCC relief maps (Figure S4) than in their $\nabla^2\rho$ contour maps. Nevertheless, cusps are discernible on the Xe atoms that correspond to the combined charge concentrations of the Xe VELPS, whereas the O VELPS are not discernible. Small charge concentration cusps are visible between the Xe and O atoms. In the case of FXeOXeOXeF and $[XeOXeOXe][\mu\text{-}F(ReO_2F_3)_2]_2$, cusps between F and Xe are not clearly distinguishable.

Electron Localization Function (ELF) Analyses. ELF analyses were carried out for $[XeOXeOXe]^{2+}$ (C_{2h}), FXeOXeOXeF (C_i), and $[XeOXeOXe][\mu\text{-}F(ReO_2F_3)_2]_2$ (C_i) primarily to visualize the behaviors of the Xe VELPs of these species. In the ensuing discussion, the following abbreviations denote an atomic basin population, $\bar{N}[A]$; the electron localization function, $\eta(\mathbf{r})$; a core basin, C(A); a monosynaptic valence basin, V(A); and a closed isosurface value, $\eta(\mathbf{r}) = f$, at which a specific isosurface can be visualized. ELF parameters are provided in Tables 5 and S9, and ELF isosurface plots at the isosurface contour value $\eta(\mathbf{r}) = 0.60$ are shown for the localization domains of $[XeOXeOXe]^{2+}$, $[XeOXeOXe][\mu\text{-}F(ReO_2F_3)_2]_2$, and FXeOXeOXeF in Figures 4 and S5.

The ELF population analyses (Tables 5 and S9) are in agreement with the QTAIM results (see above). The ELF basin populations of the $Xe_{(1)}$ and $Xe_{(2,2A)}$ cores are comparable for $[XeOXeOXe]^{2+}$, FXeOXeOXeF, and the ion pair. In all cases, the $Xe_{(1)}$ and $Xe_{(2,2A)}$ core populations are close to the ideal core population of the Xe atom, [Kr] $4d^{10}$ = 46 e. The ELF valence population analyses suggest an interpretation of the bonding in terms of a significant delocalization of electron density between the valence shells of Xe and those of its neighboring atoms. Overall, the electron density transfer from the xenon atoms to O in free $[XeOXeOXe]^{2+}$ and to F and O in FXeOXeOXeF and the ion pair leads to O and F valence population increases of 0.5 to 0.9 e, consistent with semi-ionic bonding. A similar interpretation applies to the bonding in XeF_2[65] and KrF_2.[66]

The localization domain reduction tree diagrams[67] provide the hierarchies of the ELF basins and the corresponding basin separation values (f_{sep}) for $[XeOXeOXe]^{2+}$, FXeOXeOXeF, and $[XeOXeOXe][\mu\text{-}F(ReO_2F_3)_2]_2$ (Figure 5). The ELF reduction of localization diagram of $[XeOXeOXe][\mu\text{-}F(ReO_2F_3)_2]_2$ shows that the ion pair initially separates (f_{sep} = 0.10) into $[XeOXeOXe][Re_{(1,1A)}O_2F_4]_2$ and two $Re_{(2,2A)}O_2F_3$ f-localization domains. The former separates (f_{sep} = 0.15) into $V(F_{(2,2A)})$ and the $[XeOXeOXe][\mu\text{-}F_{(1,1A)}(Re_{(1,1A)}O_2F_2)]_2$ f-localization domain. The latter subsequently separates (f_{sep} = 0.20) into $V(F_{(1,1A)})$, and the $Re_{(1,1A)}O_2F_2$ and XeOXeOXe f-localization domains. The XeOXeOXe domain separates (f_{sep} = 0.39) into $V(Xe_{(1)})$ and the $Xe_{(2,2A)}O_{(1,1A)}$ f-localization domains, which finally separate (f_{sep} = 0.46) into $V(Xe_{(2,2A)})$ and $V(O_{(1,1A)})$. For comparison, the XeOXeOXe domain separates at similar values for $[XeOXeOXe]^{2+}$ (f_{sep} = 0.39) and FXeOXeOXeF (f_{sep} = 0.41), whereas $V(Xe_{(2,2A)})$ and $V(O_{(1,1A)})$ separate at f_{sep} = 0.51 for $[XeOXeOXe]^{2+}$ and at f_{sep} = 0.42 for FXeOXeOXeF. The earlier separations of the $V(Xe_{(1)})$ basins from their XeOXeOXe domains relative to those of $V(Xe_{(2,2A)})$ is consistent with central $Xe_{(1)}-O_{(1,1A)}$ bonds that are more ionic than the terminal $Xe_{(2,2A)}-O_{(1,1A)}$ bonds and with resonance structures (**1**) and (**2**), their NBO analyses (Tables 4 and S8), and the QTAIM findings (Table 5). The ELF isosurface values at which the $V(F_{(1,1A)})$ valence basins separate ($[XeOXeOXe][\mu\text{-}F(ReO_2F_3)_2]_2$, f_{sep} = 0.20; FXeOXeOXeF, f_{sep} = 0.31) are consistent with the lower covalent characters of the $Xe_{(2,2A)}$---$F_{(1,1A)}$ bridge bonds in the ion pair relative to those of the $Xe_{(2,2A)}-F_{(1,1A)}$ bonds in FXeOXeOXeF and their respective bond orders obtained from the NBO analyses, i.e., $[XeOXeOXe][\mu\text{-}F(ReO_2F_3)_2]_2$ (0.141) and FXeOXeOXeF (0.259).

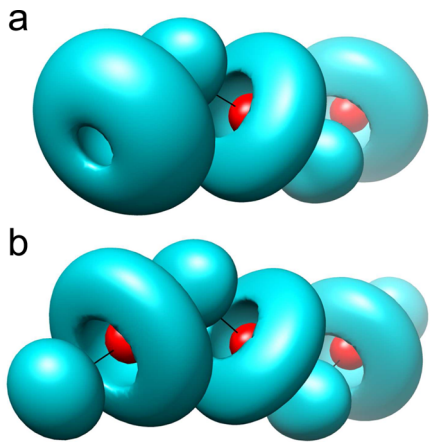

Figure 4. ELF isosurface plots at $\eta(\mathbf{r})$ = 0.60 (B3LYP/aug-cc-pVDZ(-PP)) for (a) $[XeOXeOXe]^+$ and (b) [FXeOXeOXeF]. Color code: red = core; blue = monosynaptic basin. See Figure S5 for other orientations and for the ELF isosurface plot of $[XeOXeOXe][\mu\text{-}F(ReO_2F_3)_2]_2$.

The Xe valence basins consist of the toroidal-shaped valence electron densities resulting from the combination of the three nonbonding VELP domains of Xe with exposed atomic core densities at their centers. Such torus-shaped basins have been calculated for XeF_2,[65,68] $[XeF_3]^-$,[68] $[XeOTeF_5]^+\cdot SO_2ClF$,[50] and for the NgF_2 (Ng = Kr or Xe) ligands in $[BrOF_2][AsF_6]\cdot 2NgF_2$.[65,66] Variations in VELP behavior have been noted for the NgF_2 adducts of the $[BrOF_2]^+$ cation in $[BrOF_2][AsF_6]\cdot 2NgF_2$, where NgF_2 and $[AsF_6]^-$ are fluorine bridged to Br(V). In this case, the Br(V) valence basin is an electron lone pair that accommodates its shape and volume to the environment available to it in its complex. This contrasts with the Br(V) VELP of the free cation, $[BrOF_2]^+$, which is dramatically expanded in its less constrained environment.

In the present series, the volumes of the toroidal $V(Xe_{(1)})$ and $V(Xe_{(2,2A)})$ valence basins ($\eta(\mathbf{r})$ = 0.60) increase with

DOI: 10.1021/jacs.5b08765
J. Am. Chem. Soc. 2015, 137, 13398−13413

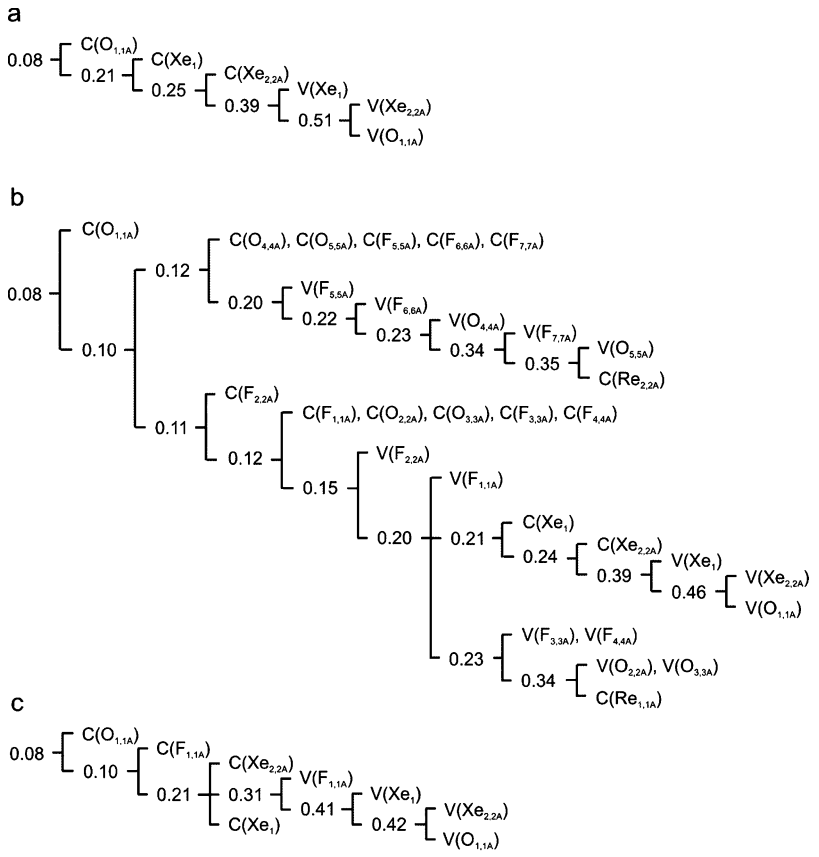

Figure 5. Reduction of the localization diagrams for (a) $[XeOXeOXe]^{2+}$, (b) $[XeOXeOXe][\mu\text{-}F(ReO_2F_3)_2]_2$, and (c) FXeOXeOXeF showing the ordering of localization nodes and the boundary isosurface values, $\eta(\mathbf{r})$ (also referred to as f_{sep} values), at which the reducible domains split.

decreasing NBO charge of the XeOXeOXe moiety, i.e., $[XeOXeOXe]^{2+}$ (1.88 Å^3 ($Xe_{(1)}$), 1.93 Å^3 ($Xe_{(2,2A)}$); +2.00), $[XeOXeOXe][\mu\text{-}F(ReO_2F_3)_2]_2$ (2.41 Å^3 ($Xe_{(1)}$), 2.86 Å^3 ($Xe_{(2,2A)}$); +1.67), FXeOXeOXeF (3.01 Å^3 ($Xe_{(1)}$), 3.37 Å^3 ($Xe_{(2,2A)}$); +1.23). Plots of the xenon valence basin volumes versus charge are near-linear for both the terminal and central xenon valence basin volumes. In all three cases, the volume of $V(Xe_{(2,2A)})$ is larger than that of $V(Xe_{(1)})$. In general, the valence basin of the central $Xe_{(1)}$ atom is symmetrically bonded to oxygen and is more confined than the corresponding $Xe_{(2,2A)}$ valence basins. In FXeOXeOXeF, where the $Xe_{(2,2A)}$–$F_{(1,1A)}$ bonds are stronger and more confining than the $Xe_{(2,2A)}$---$F_{(1,1A)}$ bridge bonds of $[XeOXeOXe][\mu\text{-}F(ReO_2F_3)_2]_2$, the terminal and central Xe valence basins are the most symmetric and their toroidal holes most open, exposing the $Xe_{(2,2A)}$ core charges for interaction with the $F_{(1,1A)}$ ligands of the anions. The similar shapes of the $Xe_{(1)}$ and $Xe_{(2,2A)}$ tori of FXeOXeOXeF are consistent with their similar bonding environments and abilities to confine their Xe VELP volumes and shapes. The $Xe_{(2,2A)}$ tori of the ion pair are considerably more expanded, and their valence holes more contracted, in accordance with the asymmetries that result from their weaker $Xe_{(2,2A)}$---$F_{(1,1A)}$ interactions. The $Xe_{(2,2A)}$ tori of the free $[XeOXeOXe]^{2+}$ cation, where the isosurface is the least confined, are the most asymmetric among the series, standing in marked contrast to those of FXeOXeOXeF and the ion pair. The $Xe_{(2,2A)}$ tori of $[XeOXeOXe]^{2+}$ are significantly contracted at the extremities of the cation, giving somewhat conical-shaped tori and significantly narrowed toroidal holes that correspond to σ-holes (see MEPS discussion).

Similar bonding modalities arise for the $[FNgNCH]^+$ cations (Ng = Kr or Xe), as described in 1989 by MacDougall, Bader, and Schrobilgen,[69] where the Lewis acid behaviors of the $[NgF]^+$ cations toward HCN were also shown to be due to the presence of holes in the valence shells of charge concentrations for Kr(II) and Xe(II) which expose their Ng cores to the nitrogen VELP of HCN.

Molecular Electrostatic Potential Surface (MEPS) Analyses. The MEPSs of the $[XeOXeOXe]^{2+}$ cation, FXeOXeOXeF, and the $[XeOXeOXe][\mu\text{-}F(ReO_2F_3)_2]_2$ ion pair have been calculated at the 0.001 electron bohr^{-3} contour level. The color scale used in Figure 6a differs from that used in Figure 6b,c, whereas the energy scales are directly comparable. The $[XeOXeOXe]^{2+}$ cation displays high positive electrostatic potentials on the terminal $Xe_{(2,2A)}$ atoms (895 kJ mol^{-1}) and between the $Xe_{(1)}$ and $Xe_{(2,2A)}$ atoms (901 kJ mol^{-1}) (Figure 6a). The most positive electrostatic potentials occur between $Xe_{(1)}$ and $Xe_{(2,2A)}$ and are opposed to the lowest electrostatic potential values which are located on the O atoms (635 kJ mol^{-1}). The highest electrostatic potentials on the $Xe_{(2,2A)}$ atoms are opposite to the $Xe_{(2,2A)}$–O bonds and correspond to highly directional σ-holes.[70−74] In the ELF analysis described above, the σ-holes correspond to the exposed $Xe_{(2,2A)}$ cores situated at the centers of the toroidal $Xe_{(2,2A)}$ valence basins.

The formation of the hypothetical FXeOXeOXeF molecule by donation of a F^- VELP into the σ-hole of each $Xe_{(2,2A)}$ atom results in electrostatic potentials that are lower than those of $[XeOXeOXe]^{2+}$. The highest electrostatic surface potential still occurs between $Xe_{(1)}$ and $Xe_{(2,2A)}$ (151 kJ mol^{-1}), whereas the lowest electrostatic surface potentials now occurs on the

DOI: 10.1021/jacs.5b08765
J. Am. Chem. Soc. 2015, 137, 13398−13413

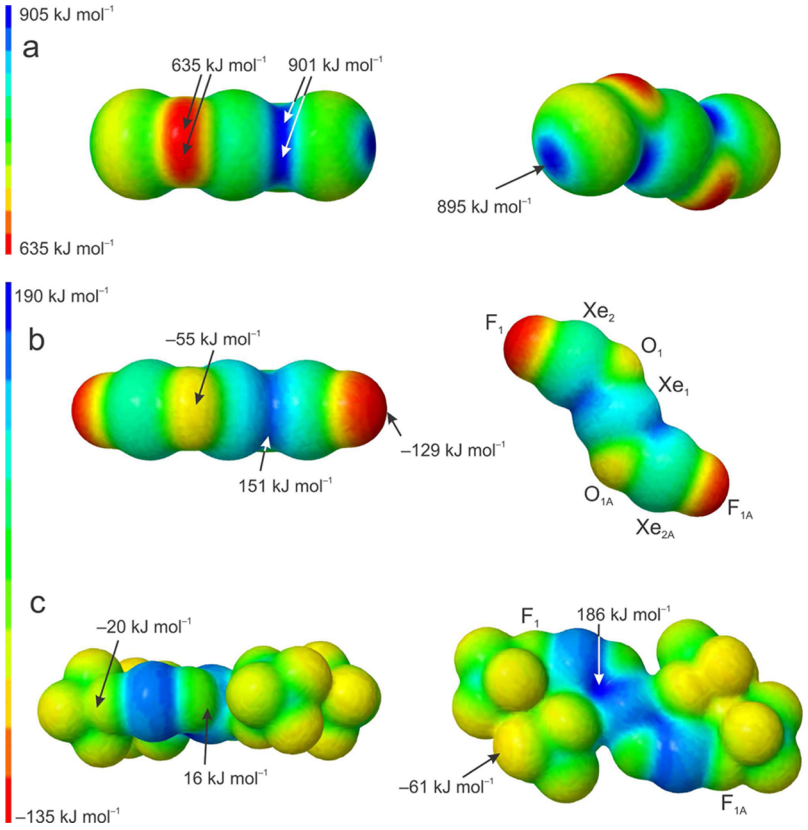

Figure 6. Calculated molecular electrostatic potentials at the 0.001 electron bohr^{-3} surfaces of (a) the $[XeOXeOXe]^{2+}$ cation, (b) FXeOXeOXeF, and (c) the $[XeOXeOXe][\mu\text{-}F(ReO_2F_3)_2]_2$ ion pair. The color scales range from red (−905 kJ mol^{-1}) to blue (635 kJ mol^{-1}) for $[XeOXeOXe]^{2+}$ and from red (−135 kJ mol^{-1}) to blue (190 kJ mol^{-1}) for FXeOXeOXeF and $[XeOXeOXe][\mu\text{-}F(ReO_2F_3)_2]_2$. Maximum and minimum electrostatic potentials are indicated by arrows. The optimized geometries and molecular surface electrostatic potentials were calculated at the B3LYP/aug-cc-pVDZ(-PP) level of theory.

terminal fluorine atoms (−129 kJ mol^{-1}). The electrostatic surface potentials of the fluorine-bridged $[XeOXeOXe]^{2+}$ cation of $[XeOXeOXe][\mu\text{-}F(ReO_2F_3)_2]_2$ are somewhat higher than those of FXeOXeOXeF, but are significantly lower than those of the naked $[XeOXeOXe]^{2+}$ cation. This is corroborated by the NBO analyses (see NBO Analyses), which show that the total charge of the XeOXeOXe-moiety in the ion pair is significantly greater than that of the FXeOXeOXeF molecule. The most negative electrostatic potential values on the isosurfaces of the bridging fluorines of the ion pair (−20 kJ mol^{-1}) are significantly more positive than those of the terminal F atoms of FXeOXeOXeF (−129 kJ mol^{-1}) and the $[\mu\text{-}F(ReO_2F_3)_2]^-$ anions (−61 to −32 kJ mol^{-1}). This observation is consistent with the ionic formulation of $[XeOXeOXe][\mu\text{-}F(ReO_2F_3)_2]_2$ in its crystal structure.

CONCLUSION

The low-temperature synthesis of a kinetically stable salt of the novel $[XeOXeOXe]^{2+}$ cation has been accomplished by reaction of ReO_3F with XeF_2 in aHF. The synthetic approach is reliant upon ReO_3F as the oxygen source and as the progenitor of the counterion, $[\mu\text{-}F(ReO_2F_3)_2]^-$. The reaction pathway likely involves HOXeF as an intermediate in a series of oxygen/fluorine metathesis steps that lead to $[XeOXeOXe]^{2+}$ and the $[\mu\text{-}F(ReO_2F_3)_2]^-$ anion. The $[XeOXeOXe][\mu\text{-}F(ReO_2F_3)_2]_2$ salt is the first instance where the $[\mu\text{-}F(ReO_2F_3)_2]^-$ anion has been used to stabilize a strong oxidant cation. The $[XeF_5]^+$ and $[Xe_2F_{11}]^+$ cations are the only other noble-gas cations to have been stabilized by metal oxide fluoride anions, namely, $[XeF_5][\mu\text{-}F(OsO_3F_2)_2]$ and $[M][fac\text{-}OsO_3F_3]$ ($[M]^+ = [XeF_5]^+$, $[Xe_2F_{11}]^+$).[61]

The $[XeOXeOXe]^{2+}$ cation is unique in several respects. Its discovery provides the first examples of a xenon(II) oxide, a noble-gas oxide cation, and a rare example of a noble-gas dication.[75] It is also the first noble-gas dication for which a crystal structure is available. Not only has $[XeOXeOXe][\mu\text{-}F(ReO_2F_3)_2]_2$ been unambiguously characterized by low-temperature single-crystal X-ray diffraction, but its Raman spectrum and vibrational assignments have been confirmed by quantum-chemical calculations and ^{18}O-enrichment studies.

The Xe−O and Xe−F bonding in free $[XeOXeOXe]^{2+}$, the hypothetical neutral oxide fluoride, FXeOXeOXeF, and the ion pair, $[XeOXeOXe][\mu\text{-}F(ReO_2F_3)_2]_2$, were studied with the aid of NBO, QTAIM, ELF, and MEPS analyses. The Xe−O bonds of $[XeOXeOXe]^{2+}$ are semi-ionic, with the terminal Xe−O bonds exhibiting more covalent character. The terminal Xe atoms of $[XeOXeOXe]^{2+}$ show regions of high positive electrostatic potential, opposite to their Xe−O bonds, which correspond to σ-holes. The cation−anion F bridge interaction can be accounted for in terms of a σ-hole bond, where F atoms of the anions donate electron density to the electrophilic regions (σ-holes) of the terminal Xe atoms. As shown by the NBO, QTAIM, and ELF analyses, the Xe---F bridge bonds are weakly covalent and consistent with a true ion-pair and σ-hole bonds.

DOI: 10.1021/jacs.5b08765
J. Am. Chem. Soc. 2015, 137, 13398−13413

EXPERIMENTAL SECTION

Apparatus and Materials. Manipulations involving air-sensitive materials were carried out under anhydrous conditions on glass and metal high-vacuum lines and inside an inert atmosphere drybox as previously described.[76] All synthetic work was carried out in vessels constructed from $^1/_4$-in. o.d. lengths of FEP fluoroplastic tubing. The tubing was heat-sealed at one end, heat flared, and connected through a 45° SAE flare nut to the conical end of a Kel-F valve to form a compression seal. Reaction vessels were initially dried on a Pyrex glass vacuum line and then transferred to a metal vacuum line where they were passivated with ca. 1000 Torr of F_2 for several hours, refilled with dry N_2, and stored in a drybox until used. All vacuum line connections were made by use of $^1/_4$-in. 316 stainless steel Swagelok Ultratorr unions fitted with Viton O-rings.

Anhydrous HF (Matheson) was purified as previously described.[77] Xenon difluoride, XeF_2,[78] and ReO_3F[40] were synthesized as previously described. The synthesis of ^{18}O-enriched Re_2O_7 was achieved by combustion of Re powder (Cleveland Refractory Metals, 325 mesh) in $^{18}O_2$ (Isotec, Inc.; 95−99% ^{18}O) and was similar to that previously described for the synthesis of natural abundance Re_2O_7.[40] The synthesis of $Re_2{}^{18}O_7$ was carried out at approximately one-eighth scale.

Synthesis of [XeOXeOXe][μ-F(ReO$_2$F$_3$)$_2$]$_2$. The salt, [XeOXeOXe][μ-F(ReO_2F_3)$_2$]$_2$, was synthesized by reaction of XeF_2 with ReO_3F (eqs 1−5). A range of reactant ratios was explored to determine if other xenon(II) oxide cations could be formed; however, only [XeOXeOXe][μ-F(ReO_2F_3)$_2$]$_2$ was isolated. The following molar ratios of reactants were investigated: XeF_2: ReO_3F = 2.11:1.00, [0.1208 g, 0.7136 mmol: 0.0857 g, 0.3385 mmol]; 1.19:1.00, [0.0570 g, 0.3366 mmol: 0.0694 g, 0.2827 mmol]; 1.18:1.00, [0.0893 g, 0.5275 mmol: 0.1132 g, 0.4471 mmol], 1.14:1.00 [0.0638 g, 0.3769 mmol: 0.0839 g, 0.3315 mmol], 1.02:1.00 [0.0546 g, 0.3222 mmol: 0.0805 g, 0.3179 mmol], and 0.56:1.00 [0.0361 g, 0.2131 mmol: 0.0964 g, 0.3806 mmol]; XeF_2: $Re^{18}O_3F$ = 1.00:0.66, [0.1706 g, 1.007 mmol: 0.1701 g, 0.6717 mmol].

The general synthetic procedure follows: Anhydrous HF (ca. 0.3 mL) was condensed into a $^1/_4$-in. o.d. FEP reactor at −196 °C. Inside a drybox, aHF was frozen in a metal Dewar filled with 4.5 mm copper plated steel spheres (air rifle shot) that had been cooled to ca. −140 °C in the glass cryowell of the drybox with liquid N_2. Rhenium trioxide fluoride, ReO_3F, was weighed into the reactor, and its frozen contents were briefly warmed to room temperature whereupon ReO_3F dissolved to form a pale yellow solution. The solution was immediately refrozen at −140 °C, and XeF_2 was weighed into the reactor. The reactor and its frozen contents were rapidly removed from the drybox and warmed to −30 °C at which temperature the reactants dissolved over a period of ca. 5−10 min forming a pale-yellow solution. As the reaction proceeded to completion (2−4 h), the solution color changed to bright yellow-orange. Upon completion of the reaction, a red-orange, microcrystalline powder irreversibly precipitated, and the supernatant decolorized when the yellow-orange solution was cooled to −78 °C. Low-temperature Raman spectra were obtained for the dry red-orange solids that formed when XeF_2 and ReO_3F (2.11:1.00, 1.18:1.00) had fully reacted. The solids were isolated by removal of HF under dynamic vacuum at −78 °C and were assigned to [XeOXeOXe][μ-F(ReO_2F_3)$_2$]$_2$.

Low-temperature Raman spectra were also recorded for the red-orange solids that formed when XeF_2 and ReO_3F (1.19:1.00, 1.14:1.00) were only partially reacted at −30 °C. The red-orange precipitates were obtained when the reaction mixtures were cooled to −78 °C (see above) and frozen under their yellow-orange supernatants at −140 °C. The frozen supernatants contained unreacted XeF_2 and $ReO_3F(FH)_2$, which were not observed when the laser was focused on the red-orange precipitates. The Raman spectra of the dry products and those recorded under the frozen HF solutions were identical and were assigned to [XeOXeOXe][μ-F(ReO_2F_3)$_2$]$_2$. The solution samples were subsequently slowly warmed to room temperature for ca. 5 min, whereupon they decomposed. Their solute mixtures were isolated by removal of HF and residual XeF_2 under dynamic vacuum at room temperature. The Raman spectra of the resulting mixtures corresponded to ReO_2F_3 and unreacted ReO_3F.

The decomposition of solid [XeOXeOXe][μ-F(ReO_2F_3)$_2$]$_2$ was also investigated. The product was obtained from the reaction of a 1:1.33 molar ratio of XeF_2:ReO_3F [0.0689 g, 0.4068 mmol: 0.1373 g, 0.5423 mmol] in aHF and was isolated by removal of HF under dynamic vacuum at −78 °C. Warming the solid to room temperature for 1 h resulted in a solid, white mixture. The Raman spectrum of the mixture corresponded to ReO_2F_3 and XeF_2.

X-ray Crystallography. *Crystal Growth and Crystal Mounting.* Crystals of [XeOXeOXe][μ-F(ReO_2F_3)$_2$]$_2$ were grown in $^1/_4$-in. o.d. FEP reaction vessels equipped with side arms to give T-shaped reaction vessels that were fitted with Kel-F valves.[60] Crystals grew as red-orange plates upon cooling bright yellow-orange HF solutions of XeF_2:ReO_3F (0.56:1.00 and 1.02:1.00) from −30 to −35 °C in a low-temperature bath over a 5 h period under ca. 1 atm of dry nitrogen. Upon completion of crystal growth, the supernatants were decanted into the side arms of the reactors, which had been cooled to −196 °C. The crystalline products were dried under dynamic vacuum at −50 °C before the side arms containing the frozen supernatants were heat-sealed off under dynamic vacuum. The crystalline products were stored at −78 °C under 1 atm of dry nitrogen until suitable crystals could be mounted on the X-ray diffractometer. Crystals were selected at −105 ±3 °C for low-temperature X-ray structure determinations and were mounted in a cold stream (−173 °C) on a goniometer head as previously described.[79] Red-orange colored plates having the dimensions 0.045 × 0.058 × 0.097 mm^3 (XeF_2:ReO_3F = 0.56:1.00) and 0.052 × 0.176 × 0.320 mm^3 (XeF_2:ReO_3F = 1.02:1.00) were selected for structure determinations. The structure obtained from the former crystal is reported in this work.

Collection and Reduction of X-ray Data. Crystals were centered on a Bruker SMART APEX II diffractometer, equipped with an APEX II 4K CCD (charge-coupled device) area detector and a triple-axis goniometer, and controlled by the APEX II Graphical User Interface (GUI) software.[80] A Bruker Triumph curved crystal monochromator was used with a Mo Kα (λ = 0.71073 Å) radiation source. Diffraction data collection at −173 °C consisted of ω-scans (4040 images) collected at 0.5° intervals at fixed χ = 54.74°. The crystal-to-detector distances were 4.954 cm for both crystals, and the data collections were carried out in a 512 × 512 pixel mode using 2 × 2 pixel binning. Processing of the raw data sets was completed by using the APEX II GUI software,[80] which applied Lorentz and polarization corrections to the three-dimensionally integrated diffraction spots. The program, SADABS,[81] was used for scaling the diffraction data, the application of decay corrections, and empirical absorption corrections based on the intensity ratios of redundant reflections.

Solution and Refinement of the Structure. The XPREP[82] program was used to confirm the crystal lattice as well as the space group. The structure was solved in the centrosymmetric space group, $P\bar{1}$, by use of direct methods which located the positions of the Re and Xe atoms in the crystal structures. The positions of all fluorine and oxygen atoms were revealed in successive difference Fourier syntheses.

Refinement of the crystal structure of [XeOXeOXe][μ-F(ReO_2F_3)$_2$]$_2$ was straightforward. The final refinement was obtained by introducing anisotropic thermal parameters and the recommended weightings for all of the atoms. The maximum electron densities in the final difference Fourier maps were located near the heavy atoms. All calculations were performed using the SHELXTL-plus package[82] for the structure determinations, solution refinements, and molecular graphics. The space group choice was confirmed using Platon from the WinGX software package.[83]

Raman Spectroscopy. Low-temperature (−140 °C) Raman spectra were recorded on a Bruker RFS 100 FT Raman spectrometer using 1064-nm excitation and a resolution of 1 cm^{-1} as previously described.[79] The spectra were recorded using a laser power of 500 mW, and a total of 1200 scans were collected for the spectra of natural abundance and ^{18}O-enriched [XeOXeOXe][μ-F(ReO_2F_3)$_2$]$_2$.

Computational Details. All calculations were performed using the Gaussian 09[84] (geometry optimization and vibrational frequencies and intensities) software packages. Geometries were fully optimized using

DOI: 10.1021/jacs.5b08765
J. Am. Chem. Soc. 2015, 137, 13398−13413

density functional theory (B3LYP and PBE1PBE) and the aug-cc-pVDZ (O and F) and aug-cc-pVDZ-PP (Re and Xe) basis sets. The combined use of aug-cc-pVDZ and aug-cc-pVDZ-PP basis sets is indicated as aug-cc-pVDZ(-PP). All basis sets were obtained online from the EMSL Basis Set Exchange (https://bse.pnl.gov/bse/portal).[85] Fundamental vibrations were calculated for the optimized structures. NBO analyses were performed with the NBO program (version 6.0).[86] The MEPS were calculated using the cubegen utility as implemented in G09 and formatted Gaussian 09 checkpoint files as input. The G09 checkpoint files were created upon optimization of the geometries at the B3LYP (PBE1PBE)/aug-cc-pVDZ(-PP) levels. AIM and ELF analyses were performed as implemented in the Multiwfn package,[87] using formatted Gaussian 09 wave function files as input. The G09 wave function files were created by performing single-point calculations at the B3LYP (PBE1PBE)/aug-cc-pVDZ(-PP) levels of theory on optimized geometries. The GaussView[88] program was used to visualize the vibrational displacements that form the basis for the vibrational mode descriptions given in Tables 3 and S3–S6. The MEPS and NBO diagrams were drawn with Jmol[89] and Chimera,[90] respectively.

■ ASSOCIATED CONTENT

Supporting Information

The Supporting Information is available free of charge on the ACS Publications website at DOI: 10.1021/jacs.5b08765.

Experimental and calculated geometrical parameters for $[XeOXeOXe][\mu\text{-}F(ReO_2F_3)_2]_2$, $[XeOXeOXe]^{2+}$, $[\mu\text{-}F(ReO_2F_3)_2]^-$, and FXeOXeOXeF (Table S1); crystal packing in $[XeOXeOXe][\mu\text{-}F(ReO_2F_3)_2]_2$ (Figure S1); intermolecular contacts in the crystal structure of $[XeOXeOXe][\mu\text{-}F(ReO_2F_3)_2]_2$ (Figure S2); selected bond lengths and corresponding valences for $[XeOXeOXe][\mu\text{-}F(ReO_2F_3)_2]_2$ (Table S2); experimental and calculated vibrational frequencies for $[Xe^{16/18}OXe^{16/18}OXe][\mu\text{-}F(Re^{16/18}O_2F_3)_2]_2$ (Tables S3 and S4); calculated vibrational frequencies for $[Xe^{16/18}OXe^{16/18}OXe]^{2+}$ (Table S5), $[\mu\text{-}F(Re^{16/18}O_2F_4)]^-$ (Table S6), and FXeOXeOXeF (Table S7); calculated structures of $[XeOXeOXe]^{2+}$, FXeOXeOXeF, and $[\mu\text{-}F(ReO_2F_3)_2]^-$ (Figure S3); NBO (Table S8) and QTAIM (Table S9) data for $[XeOXeOXe][\mu\text{-}F(ReO_2F_3)_2]_2$, $[XeOXeOXe]^{2+}$, and FXeOXeOXeF; relief maps ($-\nabla^2\rho$) for $[XeOXeOXe][\mu\text{-}F(ReO_2F_3)_2]_2$, $[XeOXeOXe]^{2+}$, and FXeOXeOXeF (Figure S4); and ELF isosurface plots for $[XeOXeOXe]^{2+}$, FXeOXeOXeF, and $[XeOXeOXe][\mu\text{-}F(ReO_2F_3)_2]_2$ (Figure S5) (PDF)

X-ray crystallographic file for the structure determination of $[XeOXeOXe][\mu\text{-}F(ReO_2F_3)_2]_2$ (CIF)

■ AUTHOR INFORMATION

Corresponding Author

*schrobil@mcmaster.ca

Notes

The authors declare no competing financial interest.

■ ACKNOWLEDGMENTS

We thank the Natural Sciences and Engineering Research Council of Canada for support in the form of a Discovery Grant (G.J.S.), and for an Alexander Graham Bell Canada Graduate Scholarship, NSERC-CGSD (M.V.I.), and the computational resources provided by SHARCNet (Shared Hierarchical Academic Research Computing Network; www.sharcnet.ca). We also thank Prof. Tian Lu, Beijing Kein Research Center for Natural Sciences, Beijing, P. R. China for his generous advice and guidance related to AIM and ELF calculations as implemented in Multiwfn 3.3.8.

■ REFERENCES

(1) Bartlett, N. *Proc. Chem. Soc.* **1962**, 218.
(2) Brock, D. S.; Schrobilgen, G. J.; Žemva, B. In *Comprehensive Inorganic Chemistry II*; Reedijk, J., Poepplemeier, K., Eds.; Elsevier: Oxford, U.K., 2013, Vol. *1*, pp 755–822.
(3) Brock, D. S.; Schrobilgen, G. J. *J. Am. Chem. Soc.* **2011**, *133*, 6265–6269.
(4) Smith, D. F. *J. Am. Chem. Soc.* **1963**, *85*, 816–817.
(5) Templeton, D. H.; Zalkin, A.; Forrester, J. D.; Williamson, S. M. *J. Am. Chem. Soc.* **1963**, *85*, 817.
(6) Gunn, S. R. In *Noble-Gas Compounds*; Hyman, H. H., Ed.; University of Chicago Press: Chicago, IL, 1963; pp 149–151.
(7) Appelman, E. H.; Malm, J. G. *J. Am. Chem. Soc.* **1964**, *86*, 2141–2148.
(8) Claassen, H. H.; Knapp, G. *J. Am. Chem. Soc.* **1964**, *86*, 2341–2342.
(9) Spittler, T. M.; Jaselskis, B. *J. Am. Chem. Soc.* **1965**, *87*, 3357–3360.
(10) Selig, H.; Claassen, H. H.; Chernick, C. L.; Malm, J. G.; Huston, J. L. *Science* **1964**, *143*, 1322–1323.
(11) Huston, J. L.; Studier, M. H.; Sloth, E. N. *Science* **1964**, *143*, 1161–1162.
(12) Gunn, S. R. *J. Am. Chem. Soc.* **1965**, *87*, 2290–2291.
(13) Gundersen, G.; Hedberg, K.; Huston, J. L. *J. Chem. Phys.* **1970**, *52*, 812–815.
(14) Huston, J. L.; Claassen, H. H. *J. Chem. Phys.* **1970**, *52*, 5646–5648.
(15) Gerken, M.; Schrobilgen, G. J. *Inorg. Chem.* **2002**, *41*, 198–204.
(16) Vent-Schmidt, T.; Goettel, J. T.; Schrobilgen, G. J.; Riedel, S. *Chem. - Eur. J.* **2015**, *21*, 11244–11252.
(17) Siegel, S.; Gebert, E. In *Noble-Gas Compounds*; Hyman, H. H., Ed.; University of Chicago Press: Chicago, IL, 1963; pp 193–194.
(18) Hamilton, W. C.; Ibers, J. A.; Mackenzie, D. R. *Science* **1963**, *141*, 532–534.
(19) Zalkin, A.; Forrester, J. D.; Templeton, D. H.; Williamson, S. M.; Koch, C. W. *Science* **1963**, *142*, 501–502.
(20) Ibers, J. A.; Hamilton, W. C.; Mackenzie, D. R. *Inorg. Chem.* **1964**, *3*, 1412–1416.
(21) Zalkin, A.; Forrester, J. D.; Templeton, D. H.; Williamson, S. M.; Koch, C. W. *J. Am. Chem. Soc.* **1964**, *86*, 3569–3571.
(22) Zalkin, A.; Forrester, J. D.; Templeton, D. H. *Inorg. Chem.* **1964**, *3*, 1417–1421.
(23) Marcus, Y.; Cohen, D. *Inorg. Chem.* **1966**, *5*, 1740–1743.
(24) Appelman, E. H.; Williamson, S. M. *Inorg. Synth.* **1968**, *11*, 210–213.
(25) Hauck, J. *Z. Naturforsch., B: J. Chem. Sci.* **1970**, *25*, 226.
(26) Peterson, J. L.; Claassen, H. H.; Appelman, E. H. *Inorg. Chem.* **1970**, *9*, 619–621.
(27) Downey, G. D.; Claassen, H. H.; Appelman, E. H. *Inorg. Chem.* **1971**, *10*, 1817–1820.
(28) Jørgensen, C. K.; Berthou, H. *Chem. Phys. Lett.* **1975**, *36*, 432–435.
(29) Schrobilgen, G. J.; Holloway, J. H.; Granger, P.; Brevard, C. *Inorg. Chem.* **1978**, *17*, 980–987.
(30) de Waard, H.; Bukshpan, S.; Schrobilgen, G. J.; Holloway, J. H.; Martin, D. *J. Chem. Phys.* **1979**, *70*, 3247–3253.
(31) Foropoulos, J., Jr.; DesMarteau, D. D. *Inorg. Chem.* **1982**, *21*, 2503–2504.
(32) Kläning, U. K.; Appelman, E. H. *Inorg. Chem.* **1988**, *27*, 3760–3762.
(33) Shustov, L. D.; Tolmacheva, N. S.; Nabiev, Sh. Sh.; Il'in, E. K.; Klimov, V. D.; Ushakov, V. P. *Russ. J. Inorg. Chem.* **1989**, *34*, 946–949; *Zh. Neorg. Khim.* **1989**, *34*, 1677–1680.

DOI: 10.1021/jacs.5b08765
J. Am. Chem. Soc. 2015, 137, 13398–13413

(34) Forgeron, M. A. M.; Wasylishen, R. E.; Gerken, M.; Schrobilgen, G. J. *Inorg. Chem.* **2007**, *46*, 3585−3592.
(35) Lehmann, J. F.; Mercier, H. P. A.; Schrobilgen, G. J. *Coord. Chem. Rev.* **2002**, *233*−*234*, 1−39.
(36) Dunning, T. H.; Hay, P. J. *J. Chem. Phys.* **1977**, *66*, 3767−3777.
(37) Yamanishi, M.; Hirao, K.; Yamashita, K. *J. Chem. Phys.* **1998**, *108*, 1514−1521.
(38) Ault, B. S.; Andrews, L. *Chem. Phys. Lett.* **1976**, *43*, 350−352.
(39) Gerken, M.; Moran, M. D.; Mercier, H. P. A.; Pointner, B. E.; Schrobilgen, G. J.; Hoge, B.; Christe, K. O.; Boatz, J. A. *J. Am. Chem. Soc.* **2009**, *131*, 13474−13489.
(40) Ivanova, M. V.; Köchner, T.; Mercier, H. P. A.; Schrobilgen, G. J. *Inorg. Chem.* **2013**, *52*, 6806−6819.
(41) Casteel, W. J., Jr.; Dixon, D. A.; LeBlond, N.; Lock, P. E.; Mercier, H. P. A.; Schrobilgen, G. J. *Inorg. Chem.* **1999**, *38*, 2340−2358.
(42) Mootz, D.; Ohms, U.; Poll, W. *Z. Anorg. Allg. Chem.* **1981**, *479*, 75−83.
(43) Mootz, D.; Poll, W. *Z. Anorg. Allg. Chem.* **1982**, *484*, 158−164.
(44) Bondi, A. *J. Phys. Chem.* **1964**, *68*, 441−451.
(45) Brown, I. D. *The Chemical Bond in Inorganic Chemistry: The Bond Valence Model*; Oxford University Press: Oxford, 2006.
(46) Fir, B. A.; Mercier, H. P. A.; Sanders, J. C. P.; Dixon, D. A.; Schrobilgen, G. J. *J. Fluorine Chem.* **2001**, *110*, 89−107.
(47) Bartlett, N.; Wechsberg, M.; Jones, G. R.; Burbank, R. D. *Inorg. Chem.* **1972**, *11*, 1124−1127.
(48) Malischewski, M.; Seppelt, K. *Acta Crystallogr.* **2015**, *71*, 363−365.
(49) Moran, M. D.; Brock, D. S.; Mercier, H. P. A.; Schrobilgen, G. J. *J. Am. Chem. Soc.* **2010**, *132*, 13823−13839.
(50) Mercier, H. P. A.; Moran, M. D.; Sanders, J. C. P.; Schrobilgen, G. J. *Inorg. Chem.* **2005**, *44*, 49−60.
(51) Turowsky, L.; Seppelt, K. *Z. Anorg. Allg. Chem.* **1992**, *609*, 153−156.
(52) Elliot, H. St. A.; Lehmann, J. F.; Mercier, H. P. A.; Jenkins, H. D. B.; Schrobilgen, G. J. *Inorg. Chem.* **2010**, *49*, 8504−8523.
(53) Zalkin, A.; Ward, D. L.; Biagioni, R. N.; Templeton, D. H.; Bartlett, N. *Inorg. Chem.* **1978**, *17*, 1318−1322.
(54) Gillespie, R. J.; Hargittai, I. In *The VSEPR Model of Molecular Geometry*; Allyn and Bacon: Boston, MA, 1991; pp 127−130.
(55) Mercier, H. P. A.; Schrobilgen, G. J. *Inorg. Chem.* **1993**, *32*, 145−151.
(56) Supel, J.; Marx, R.; Seppelt, K. *Z. Anorg. Allg. Chem.* **2005**, *631*, 2979−2986.
(57) Bougon, R.; Buu, B.; Seppelt, K. *Chem. Ber.* **1993**, *126*, 1331−1336.
(58) LeBlond, N.; Mercier, H. P. A.; Dixon, D. A.; Schrobilgen, G. J. *Inorg. Chem.* **2000**, *39*, 4494−4509.
(59) LeBlond, N.; Dixon, D. A.; Schrobilgen, G. J. *Inorg. Chem.* **2000**, *39*, 2473−2487.
(60) Casteel, W. J., Jr.; Dixon, D. A.; Mercier, H. P. A.; Schrobilgen, G. J. *Inorg. Chem.* **1996**, *35*, 4310−4322.
(61) Hughes, M. J.; Mercier, H. P. A.; Schrobilgen, G. J. *Inorg. Chem.* **2010**, *49*, 3501−3515.
(62) Bader, R. F. W. *Atoms in Molecules: A Quantum Theory*; Oxford University Press: Oxford, 1990.
(63) Silvi, B.; Savin, A. *Nature* **1994**, *371*, 683−686.
(64) Becke, A. D.; Edgecombe, K. E. *J. Chem. Phys.* **1990**, *92*, 5397−5403.
(65) Brock, D. S.; Casalis de Pury, J. J.; Mercier, H. P. A.; Schrobilgen, G. J.; Silvi, B. *Inorg. Chem.* **2010**, *49*, 6673−6689.
(66) Brock, D. S.; Casalis de Pury, J. J.; Mercier, H. P. A.; Schrobilgen, G. J.; Silvi, B. *J. Am. Chem. Soc.* **2010**, *132*, 3533−3542.
(67) Savin, A.; Silvi, B.; Colonna, F. *Can. J. Chem.* **1996**, *74*, 1088−1096.
(68) Vasdev, N.; Moran, M. D.; Tuononen, H. M.; Chirakal, R.; Suontamo, R. J.; Bain, A. D.; Schrobilgen, G. J. *Inorg. Chem.* **2010**, *49*, 8997−9004.
(69) MacDougall, P. J.; Schrobilgen, G. J.; Bader, R. F. W. *Inorg. Chem.* **1989**, *28*, 763−769.
(70) Clark, T.; Hennemann, M.; Murray, J. S.; Politzer, P. *J. Mol. Model.* **2007**, *13*, 291−296.
(71) Legon, A. C. *Phys. Chem. Chem. Phys.* **2010**, *12*, 7736−7747.
(72) Politzer, P.; Murray, J. S.; Clark, T. *Phys. Chem. Chem. Phys.* **2010**, *12*, 7748−7757.
(73) Politzer, P.; Murray, J. S.; Clark, T. *Phys. Chem. Chem. Phys.* **2013**, *15*, 11178−11189.
(74) Kolář, M. H.; Deepa, P.; Ajani, H.; Pecina, A.; Hobza, P. *Top. Curr. Chem.* **2014**, *359*, 1−25.
(75) Frohn, H.-J.; Bilir, V.; Westphal, U. *Inorg. Chem.* **2012**, *51*, 11251−11258.
(76) Casteel, W. J., Jr.; Dixon, D. A.; Mercier, H. P. A.; Schrobilgen, G. J. *Inorg. Chem.* **1996**, *35*, 4310−4322.
(77) Emara, A. A. A.; Schrobilgen, G. J. *Inorg. Chem.* **1992**, *31*, 1323−1332.
(78) Mercier, H. P. A.; Sanders, J. C. P.; Schrobilgen, G. J.; Tsai, S. S. *Inorg. Chem.* **1993**, *32*, 386−393.
(79) Gerken, M.; Dixon, D. A.; Schrobilgen, G. J. *Inorg. Chem.* **2000**, *39*, 4244−4255.
(80) *APEX2*, release v2011.6−1; Bruker AXS Inc.: Madison, WI, 1995.
(81) Sheldrick, G. M. *SADABS (Siemens Area Detector Absorption Corrections)*, version 2.03; Siemens Analytical X-ray Instruments, Inc.: Madison, WI, 1999.
(82) Sheldrick, G. M. *SHELXTL-Plus*, release 5.1; Siemens Analytical X-ray Instruments, Inc.: Madison, WI, 1998.
(83) Spek, A. L. *J. Appl. Crystallogr.* **2003**, *36*, 7−13.
(84) Frisch, M. J.; Trucks, G. W.; Schlegel, H. B.; Scuseria, G. E.; Robb, M. A.; Cheeseman, J. R.; Scalmani, G.; Barone, V.; Mennucci, B.; Petersson, G. A.; Nakatsuji, H.; Caricato, M.; Li, X.; Hratchian, H. P.; Izmaylov, A. F.; Bloino, J.; Zheng, G.; Sonnenberg, J. L.; Hada, M.; Ehara, M.; Toyota, K.; Fukuda, R.; Hasegawa, J.; Ishida, M.; Nakajima, T.; Honda, Y.; Kitao, O.; Nakai, H.; Vreven, T.; Montgomery, J. A., Jr.; Peralta, J. E.; Ogliaro, F.; Bearpark, M.; Heyd, J. J.; Brothers, E.; Kudin, K. N.; Staroverov, V. N.; Kobayashi, R.; Normand, J.; Raghavachari, K.; Rendell, A.; Burant, J. C.; Iyengar, S. S.; Tomasi, J.; Cossi, M.; Rega, N.; Millam, N. J.; Klene, M.; Knox, J. E.; Cross, J. B.; Bakken, V.; Adamo, C.; Jaramillo, J.; Gomperts, R.; Stratmann, R. E.; Yazyev, O.; Austin, A. J.; Cammi, R.; Pomelli, C.; Ochterski, J. W.; Martin, R. L.; Morokuma, K.; Zakrzewski, V. G.; Voth, G. A.; Salvador, P.; Dannenberg, J. J.; Dapprich, S.; Daniels, A. D.; Farkas, Ö.; Foresman, J. B.; Ortiz, J. V.; Cioslowski, J.; Fox, D. J. *Gaussian 09*, revision D.01; Gaussian, Inc.: Wallingford, CT, 2009.
(85) Basis sets and pseudopotentials were obtained from the *Extensible Computational Chemistry Environment Basis set Database*, version 2/25/04; Molecular Science Computing Facility, Environmental and Molecular Science Laboratory, which is part of the Pacific Northwest Laboratory: Richland, WA, 2004.
(86) Glendening, E. D.; Badenhoop, J. K.; Reed, A. E.; Carpenter, J. E.; Bohmann, J. A.; Morales, C. M.; Landis, C. R.; Weinhold, F. *NBO 6.0*; Theoretical Chemistry Institute, University of Wisconsin: Madison, WI, 2013.
(87) Multiwfn, version 3.3.8; Lu, T.; Chen, F. *J. Comput. Chem.* **2012**, *33*, 580−592.
(88) *GaussView*, version 3.0; Gaussian Inc.: Pittsburgh, PA, 2003.
(89) *Jmol*, an open-source Java viewer for chemical structures in 3D (http://www.jmol.org/).
(90) Pettersen, E. F.; Goddard, T. D.; Huang, C. C.; Couch, G. S.; Greenblatt, D. M.; Meng, E. C.; Ferrin, T. E. *J. Comput. Chem.* **2004**, *25*, 1605−1612.

DOI: 10.1021/jacs.5b08765
J. Am. Chem. Soc. 2015, 137, 13398−13413